

HI, CO, AND DUST IN THE PERSEUS CLOUD

RYUJI OKAMOTO,¹ HIROAKI YAMAMOTO,¹ KENGO TACHIHARA,¹ TAKAHIRO HAYAKAWA,¹ KATSUHIRO HAYASHI,¹ AND YASUO FUKUI¹

¹*Department of Physics, Nagoya University, Chikusa-ku, Nagoya 464-8602, Japan*

(Received 2016 October 28; Revised 2017 March 14; Accepted 2017 March 14)

Submitted to ApJ

ABSTRACT

Comparison analyses between the gas emission data (HI 21 cm line and CO 2.6 mm line) and the *Planck/IRAS* dust emission data (optical depth at 353 GHz τ_{353} and dust temperature T_d) allow us to estimate the amount and distribution of the hydrogen gas more accurately, and our previous studies revealed the existence of a large amount of optically-thick HI gas in the solar neighborhood. Referring to this, we discuss the neutral hydrogen gas around the Perseus cloud in the present paper. By using the *J*-band extinction data, we found that τ_{353} increases as a function of the 1.3-th power of column number density of the total hydrogen (N_H), and this implies dust evolution in high density regions. This calibrated τ_{353} - N_H relationship shows that the amount of the HI gas can be underestimated to be $\sim 60\%$ if the optically-thin HI method is used. Based on this relationship, we calculated optical depth of the 21 cm line (τ_{HI}), and found that $\langle \tau_{HI} \rangle \sim 0.92$ around the molecular cloud. The effect of τ_{HI} is still significant even if we take into account the dust evolution. We also estimated a spatial distribution of the CO-to-H₂ conversion factor (X_{CO}), and we found its average value is $\langle X_{CO} \rangle \sim 1.0 \times 10^{20} \text{ cm}^{-2} \text{ K}^{-1} \text{ km}^{-1} \text{ s}$. Although these results are inconsistent with some previous studies, these discrepancies can be well explained by the difference of the data and analyses methods.

Keywords: ISM: atoms — ISM: molecules — ISM: individual objects (Perseus cloud)

arXiv:1612.07696v3 [astro-ph.GA] 23 Mar 2017

1. INTRODUCTION

The neutral atomic hydrogen (HI) 21 cm emission was discovered in the Galaxy in 1951, and has been used in order to investigate the structure of the Galaxy. It was revealed that the Galaxy has a spiral structure and is rotating at a nearly uniform velocity of $\sim 200 \text{ km s}^{-1}$ except for within $\sim 2 \text{ pc}$ from its center (e.g., Sofue 2013). The emission also brought advances in our understanding of the interstellar medium (ISM) and external galaxies. The role of hydrogen as the raw material of stars also attracted attention. In 1970's, the interstellar carbon monoxide (CO) emission at 2.6 mm was discovered and has been used as a tracer of molecular hydrogen (H_2) clouds, and a picture of the phase transition from HI to H_2 which triggers the star formation emerged. The molecular emission lines in the H_2 gas is efficient in cooling the gas which leads to release of the cloud internal energy and subsequent gravitational collapse.

Hydrogen (either atomic or molecular) accounts for the majority of the mass of the ISM; in the Galaxy, helium, which is abundant next to hydrogen, and heavier atoms account for $\sim 25\%$ and $< 1\%$ in mass, respectively. The volume number densities of the HI gas and the H_2 gas are estimated to be $\sim 1 \text{ cm}^{-3}$ and $\sim 1000 \text{ cm}^{-3}$, respectively, on average. The physical states of the neutral gas at the intermediate density around 100 cm^{-3} are not understood into detail. In order to elucidate the evolution of the galaxies, it is an important task to better understand the behavior of the hydrogen gas including the transition from HI to H_2 over a density range $1\text{--}1000 \text{ cm}^{-3}$.

Planck is an astronomical satellite which aimed at observing the cosmic microwave background (CMB), and it observed the all sky at millimeter/sub-millimeter wavelengths (e.g., *Planck* Collaboration et al. 2011a). The data obtained by *Planck* necessarily include the emission from the ISM of the Galaxy as the foreground component of the CMB. By using the *Planck* data, physical parameters of the interstellar dust such as the optical depth at 353 GHz (τ_{353}), the dust temperature (T_d), etc. are obtained, and they are available in the archival form (*Planck* Collaboration et al. 2014). These dust parameter data have relative uncertainties of $\lesssim 10\%$, and hence, we can expect that they accurately reflect the properties and states of the ISM at an angular resolution of 5 arcmin. In particular, τ_{353} is much less than 1 for all over the sky, even toward the Galactic plane, and therefore the data offer a reliable tracer of the column density of the total hydrogen atom (N_H), if the dust-to-gas ratio (DGR) is a constant.

Fukui et al. (2014, 2015) compared the *Planck* dust data and the gas emission data such as HI and CO for

the solar neighborhood. The HI 21 cm emission is generally assumed to be optically thin as written in text books. If the dust properties are uniform and DGR is a constant, it is expected that the velocity-integrated intensity of the 21 cm spectrum (W_{HI}) is proportional to τ_{353} for the data points where the CO emission is not detected. Fukui et al. (2014, 2015) however found that the correlation between them is not so good. By introducing T_d into the $\tau_{353}\text{--}W_{\text{HI}}$ correlation plot, these authors discovered that the poor correlation in the $\tau_{353}\text{--}W_{\text{HI}}$ plot is mainly due to the data points where the density is high and T_d is low. There are two main possibilities to explain this bad correlation between τ_{353} and W_{HI} ; one is the presence of optically-thick HI gas, and the other is the presence of ‘‘CO-dark H_2 gas’’, which is H_2 gas without the CO emission (e.g., Wolfire et al. 2010; *Planck* Collaboration et al. 2011b; Langer et al. 2014). Fukui et al. (2014, 2015) investigated the H_2 fractions in the hydrogen gas by referring to the UV measurements (Gillmon et al. 2006), and found that the fractions are typically $\lesssim 10\%$ toward the lines of sight whose column densities are up to at least 10^{21} cm^{-2} . That is, HI dominates H_2 , and the ‘‘CO-dark H_2 gas’’ would not be a dominant component in the local ISM. Therefore, these authors concluded that there exists a large amount of optically thick HI gas in the local ISM whose typical optical depth is ~ 1 , and the amount of the HI gas is underestimated by $\sim 50\%$ if a correction for the opacity effect is not applied. In Fukui et al. (2014, 2015), these analyses were made for the high Galactic latitude at $|b| > 15^\circ$ where the gas density is low. An open issue discussed in Fukui et al. (2014, 2015) is if τ_{353} obeys a simple linear relationship with the N_H or not. A study in the Orion A molecular cloud (Roy et al. 2013) indicates that the dust optical depth is proportional to the 1.28-th power of N_H rather than a simple linear relation. If correct, this non-linearity may be ascribed to the dust evolution at high column density. This suggests a possibility to apply a minor modification of the method of Fukui et al. (2014, 2015) in order to improve the accuracy in N_H .

The Perseus cloud is one of the well-known molecular clouds in the solar neighborhood ($d \sim 300 \text{ pc}$) located at $(\ell, b) \sim (160^\circ, -20^\circ)$ (e.g., Bally et al. 2008). This region is a part of the Gould's belt and the cloud in-

¹ Note that in Figure 16 of Fukui et al. (2015), the H_2 fractions are somewhat larger than 10% toward two Galactic B-type stars, HD 210121 and HD 102065 (Rachford et al. 2002). These two stars may be contaminated by their own localized gas, and therefore, the H_2 fractions for the local ISM are possibly not reliable toward them. For this reason, Fukui et al. (2017) (see Section 4.3) did not use the results obtained in Rachford et al. (2002).

cludes some star forming regions (SFRs), IC 348 and NGC 1333, for example. There are a few previous studies on the interstellar hydrogen gas in the Perseus region such as Lee et al. (2012, 2014) and Stanimirović et al. (2014). Lee et al. (2012, 2014) estimated a spatial distribution of the X_{CO} factor, which is a conversion factor between the velocity-integrated intensity of $^{12}\text{CO}(J=1-0)$ line (W_{CO}) and the column number density of the H_2 gas (N_{H_2}). They used the *IRAS* 60, 100 μm data, and concluded that the average value of X_{CO} is $\sim 0.3 \times 10^{20} \text{ cm}^{-2} \text{ K}^{-1} \text{ km}^{-1} \text{ s}$. This average value is significantly smaller than the typical value for the Galaxy, $(1-2) \times 10^{20} \text{ cm}^{-2} \text{ K}^{-1} \text{ km}^{-1} \text{ s}$ (e.g., Bolatto et al. 2013). In Stanimirović et al. (2014), the measurements of the optical depth of the H I gas (τ_{HI}) around the Perseus cloud were made. They observed the H I 21 cm absorption spectra toward 26 extra-Galactic radio continuum sources, and analyzed the data by using the method described in Heiles & Troland (2003). They concluded that optically-thick H I gas was detected only toward $\sim 15\%$ of the lines of sight, which disagrees with the results of Fukui et al. (2014, 2015), and cast doubt on the “optically-thick H I gas”.

With these results in mind, the aims of the present study are as follows:

- To investigate whether the arguments by Fukui et al. (2014, 2015) still hold or not in the region where the density is relatively high and there exist the SFRs, and to explore if the $\tau_{353}-N_{\text{H}}$ relationship requires the non-linear relationship, suggesting dust evolution.
- To understand the cause for the difference between the previous results by Fukui et al. (2014, 2015), and Lee et al. (2012, 2014), Stanimirović et al. (2014) on X_{CO} and τ_{HI} , and to test the validity of usage of τ_{353} in order to estimate the amount of the hydrogen gas.

The present paper is organized as follows. Section 2 introduces the data set we used in the present study, and Section 3 describes the analyses methods and the results. We present the discussions in Section 4. Finally Section 5 summarizes the paper.

2. OBSERVATIONAL DATA SET

In the present paper, we used following gas and dust maps in order to investigate relationships between them. These data were spatially smoothed to an effective HPBW (half power beam width) of 8.4 arcmin, which corresponds to that of the CfA CO data, except for the 21 cm radio continuum map (35 arcmin). Then, they

were converted to a 3.0 arcmin grid spacing in Right Ascension and Declination.

2.1. H I data

Data sets of the GALFA H I survey (Data Release 1) (Peek et al. 2011) are used in the present study. This survey was done with the Arecibo Observatory 305 m telescope, and its HPBW is ~ 4 arcmin. Note that we have linearly refitted the baseline of each spectrum using the velocity ranges of mainly $V_{\text{LSR}} \leq -161 \text{ km s}^{-1}$ and $V_{\text{LSR}} \geq +112 \text{ km s}^{-1}$ in order to correct the baseline offsets in this version of the raw GALFA data. Then, the data were spatially smoothed to be a 8.4 arcmin effective beam size, and RMS fluctuations of the smoothed data are $\sim 0.06 \text{ K}$ at a 0.18 km s^{-1} velocity resolution.

2.2. CO data

We used the $^{12}\text{CO}(J=1-0)$ data cube by Dame et al. (2001) as a tracer of H_2 gas. The HPBW is 8.4 arcmin, and the RMS noise fluctuations are $\sim 0.25 \text{ K}$ at a 0.65 km s^{-1} velocity resolution (Dame et al. 2001). We downloaded this data cube from the web site of Harvard-Smithsonian Center for Astrophysics (CfA)².

2.3. Planck and IRAS dust emission data

Archival data sets of dust optical depth at 353 GHz (τ_{353}) and dust temperature (T_{d}) obtained by *Planck* and *IRAS* satellites are used. They were obtained by fitting intensities at 353 GHz, 545 GHz, and 857 GHz observed with *Planck* and at 100 μm of IRIS (Improved Reprocessing of the *IRAS* Survey) with modified-blackbody functions (for details, see *Planck* Collaboration et al. 2011c). In the present study we utilized version R1.20 of the *Planck* dust maps³ and IRIS 60 μm and 100 μm maps⁴ (Miville-Deschênes & Lagache 2005). We downloaded all-sky FITS data sets with a HEALPix⁵ format (Górski et al. 2005).

2.4. J-band extinction data

An all-sky distribution of *J*-band extinction (A_J) was derived in Juvela & Montillaud (2016). They used “NICER” and “NICEST” methods in order to calculate the A_J map based on the 2MASS (two micron all-sky survey) *J*, *H*, and *K*-band extinction data. We downloaded an all-sky FITS data⁶ with a HEALPix format. The angular resolution of the raw map is 3 arcmin.

² <https://www.cfa.harvard.edu>

³ <http://irsa.ipac.caltech.edu>

⁴ <https://lambda.gsfc.nasa.gov>

⁵ <http://healpix.sourceforge.net>

⁶ <http://www.interstellarmedium.org>

Table 1. List of symbols used in the present paper

Symbol	Unit	Description	Note
W_{HI}	[K km s ⁻¹]	H I 21 cm line velocity-integrated intensity.	(a)
N_{HI}	[cm ⁻²]	H I column number density.	
N_{HI}^*	[cm ⁻²]	H I column number density (optically thin limit), $\equiv X_{\text{HI}} \times W_{\text{HI}}$.	
T_{HI}	[K]	H I brightness temperature.	
ΔV_{HI}	[km s ⁻¹]	H I velocity width, $\equiv W_{\text{HI}}/T_{\text{HI}}(\text{peak})$.	
τ_{HI}	...	H I optical depth.	
T_{s}	[K]	H I spin temperature.	
X_{HI}	[cm ⁻² K ⁻¹ km ⁻¹ s]	Theoretical conversion factor, $=1.823 \times 10^{18}$ cm ⁻² K ⁻¹ km ⁻¹ s.	
N_{H_2}	[cm ⁻²]	H ₂ column number density.	
N_{H}	[cm ⁻²]	Total hydrogen column number density, $=N_{\text{HI}}+2 N_{\text{H}_2}$.	
W_{CO}	[K km s ⁻¹]	¹² CO($J=1-0$) line velocity-integrated intensity.	(b)
X_{CO}	[cm ⁻² K ⁻¹ km ⁻¹ s]	Empirical CO-to-H ₂ conversion factor, $\equiv N_{\text{H}_2}/W_{\text{CO}}$.	
τ_{353}	...	Optical depth at 353 GHz derived by <i>Planck/IRAS</i> satellite.	
T_{d}	[K]	Cold dust temperature derived by <i>Planck/IRAS</i> satellite.	
A_J	[mag]	J -band extinction derived by NICEST method.	(c)
T_{bg}	[K]	Background brightness temperature at 21 cm.	(d)
$\tau_{353,\text{ref}}$...	Reference value of τ_{353} , $=1.2 \times 10^{-6}$.	(e)
$N_{\text{H},\text{ref}}$	[cm ⁻²]	Reference value of N_{H} , $=2.5 \times 10^{20}$ cm ⁻² .	(e)
α	...	Power index in Equation (2).	

NOTE— (a) Peek et al. (2011). The integrated range is from -188.4 km s⁻¹ to $+188.4$ km s⁻¹.

(b) Dame et al. (2001). The integrated range is from -4.9 km s⁻¹ to $+12.0$ km s⁻¹.

(c) Juvela & Montillaud (2016)

(d) Reich (1982); Reich & Reich (1986)

(e) Appendix A

2.5. H α data

For the purpose of identifying regions where ultraviolet (UV) emission locally affect the dust properties by heating up or destroying them, we used H α emission data. The H α map was obtained by Finkbeiner (2003) and it has an angular resolution of 6 arcmin.

2.6. 21 cm radio continuum data

21 cm continuum brightness temperature map is used in order to obtain the background emission. This map was derived by Reich & Reich (1986) and includes the 2.7 K cosmic background radiation. Although it has a lower spatial resolution (~ 35 arcmin) than the other maps, we use this map as it is in the present study.

3. ANALYSES & RESULTS

3.1. Spatial Distributions

Figure 1 shows spatial distributions of data sets used in the present study.

Figure 1(a) is the distribution of velocity-integrated intensity of ¹²CO($J=1-0$) line (W_{CO}) obtained by Dame et al. (2001). The integrated velocity range is from -4.9 km s⁻¹ to $+12.0$ km s⁻¹. We use this map as a tracer of column number densities of molecular hydrogen (N_{H_2}).

Figure 1(b) is a map of velocity-integrated intensity of H I 21 cm line (W_{HI}). It was derived by GALFA-H I survey (Peek et al. 2011). The integrated velocity range is from -188.4 km s⁻¹ to $+188.4$ km s⁻¹. Because we found some strong spike noises in the spectra in our region, we masked 4 areas to exclude these bad spectra. See Figure 2 for details on the mask.

Figure 1(c) and (d) show distributions of the dust emission parameters obtained from the *Planck/IRAS*

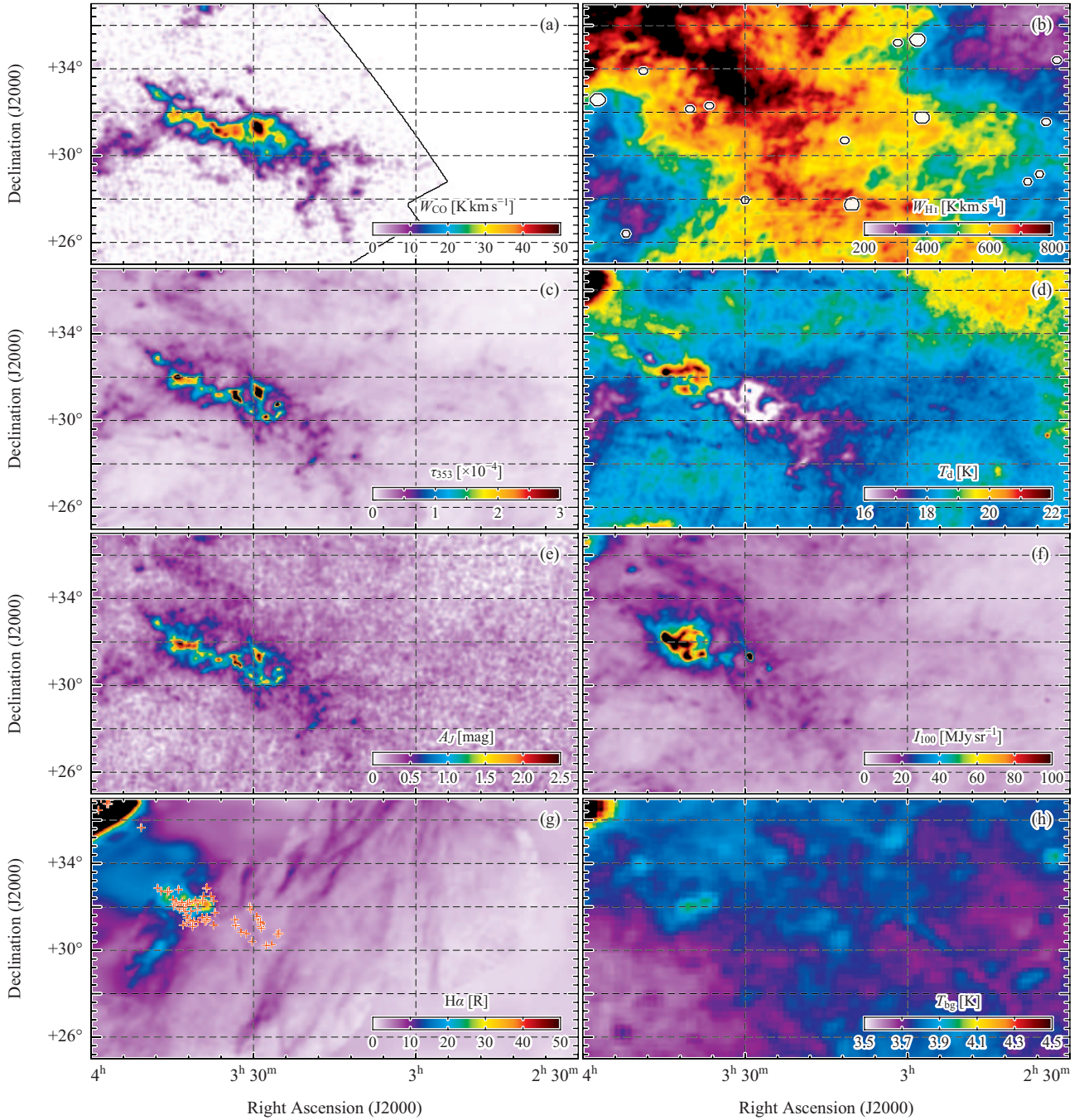


Figure 1. (a) A Velocity-integrated intensity map of $^{12}\text{CO}(J=1-0)$ line (Dame et al. 2001). The integrated velocity range is from -4.9 km s^{-1} to $+12.0 \text{ km s}^{-1}$. (b) A Velocity-integrated intensity map of H I 21 cm line (Peek et al. 2011). The integrated velocity range is from -188.4 km s^{-1} to $+188.4 \text{ km s}^{-1}$. See Figure 2 for the details of the masks. (c) and (d) Spatial distributions of optical depth at 353 GHz and cold dust temperature obtained by the *Planck/IRAS* satellites (*Planck* Collaboration et al. 2011c). (e) A map of J-band extinction derived by 2MASS data and “NICEST” analyses (Juvela & Montillaud 2016). (f) An intensity map at 100 μm obtained by *IRAS* satellite (Miville-Deschênes & Lagache 2005). (g) An H α intensity map derived by Finkbeiner (2003). Red crosses indicate positions of YSO candidates (Tóth et al. 2014). (h) A spatial distribution of the 21 cm background radio continuum (Reich & Reich 1986). This map includes the 2.7 K cosmic background radiation, etc. Effective beam sizes are 8.4 arcmin for the panels (a)–(g), and 35 arcmin for the panel (h).

observations. A map of dust optical depth at 353 GHz (τ_{353}) is drawn in Figure 1(c). τ_{353} is obtained by using the data observed with the *Planck* satellite, which is aimed at accurately detecting the spatial distribution of the CMB. Therefore, it has high reliability with typical uncertainty of $\lesssim 10\%$. In addition, the value of τ_{353} is at most $\lesssim 10^{-3}$ even toward the Galactic plane, and hence we can expect that it perfectly reflects the distribution and amount of ISM. τ_{353} is considered as a high accuracy/precision tracer of column number density of total hydrogen atoms (N_{H}) if DGR is uniform.

Figure 1(d) shows cold dust temperature (T_{d}) obtained simultaneously with τ_{353} . We can see a trend that T_{d} becomes lower toward the molecular clouds detected by CO. It indicates that dust grains themselves shield the interstellar radiation field (ISRF) in the molecular clouds and grains are less heated in addition to radiative cooling (see also Figure 5). Note that T_{d} is high around local heating sources, such as the California Nebula (NGC 1499), the Pleiades (M45), and the “ring-like feature” described in Lee et al. (2012). The T_{d} image has a relatively low contrast compared to τ_{353} , in particular the range of T_{d} in this region is typically from 17 K to 22 K. This is because T_{d} is proportional to the one-sixth power of the total intensity radiated from thermal-equilibrium grains expressed as the modified-blackbody model. It reflects that the total radiation energy of the modified-blackbody is proportional to the fourth power of the temperature, and is in addition proportional to the emissivity spectral index (~ 2).

Figure 1(e) is an image of *J*-band extinction (A_{J}) derived by (Juvela & Montillaud 2016) using 2MASS data and “NICEST” method (Lombardi & Alves 2001). We use this map as an another tracer of N_{H} .

A spatial distribution of IRIS 100 μm intensity (I_{100}) is drawn in Figure 1(f). This map is used for a comparison of the CO-to- H_2 conversion factor (see Section 4.1).

We show an intensity map of $\text{H}\alpha$ emission in Figure 1(g), overlaid with locations of young stellar object (YSO) candidates. $\text{H}\alpha$ emission indicates the presence of ionized hydrogen (HII) and thus indicates the presence of strong UV radiation. We use the data in order to identify the region where the dust may be destroyed by UV radiation. The red crosses are the location of YSO candidates catalogued by Tóth et al. (2014). From this catalogue we extracted the candidates under the condition that “probability of being a YSO candidate” is greater than 0.997. It is based on AKARI Far-Infrared Surveyor (FIS) Bright Source Catalogue.

Figure 1(h) shows a spatial distribution of brightness temperature of 21 cm continuum radiation. This map

was derived by Reich & Reich (1986) and includes the 2.7 K cosmic background radiation, etc.

3.2. Masking

Masks applied in the present study are shown in Figure (2).

- (a) This mask is used in order to mask the data points which molecular hydrogen can exist ($W_{\text{CO}} > 3\sigma$).
- (b) There exist strong spike noises (equivalent to $T_{\text{H I}} \sim 30\text{ K}$) in some spectra of GALFA-H I DR1 data. This mask is used in order to exclude the data points within 8.4 arcmin (= 1 HPBW) from these bad spectra.
- (c) In Stanimirović et al. (2014) absorption spectra due to the local H I gas are detected toward extra-Galactic radio continuum sources. Since there are 11 out of these sources in this region, this mask is used to exclude the data points within 8.4 arcmin (= 1 HPBW) from them.
- (d) This mask excludes the data points within 1.5 deg from the center of the Pleiades ($\alpha_{\text{J2000}}, \delta_{\text{J2000}} \sim (3^{\text{h}} 47^{\text{m}}, +24^{\circ} 07^{\text{m}})$) (SIMBAD Astronomical Database, Wenger et al. 2000) because dust grains are locally heated up.
- (e) Lee et al. (2012) describes the “ring-like feature”, which is formed by an H II region due to a B-type star named HD 278942 (Ridge et al. 2006). As well as Lee et al. (2012) this mask is used to exclude the data points within 56 arcmin from ($\alpha_{\text{J2000}}, \delta_{\text{J2000}} = (3^{\text{h}} 39^{\text{m}} 30^{\text{s}}, +32^{\circ})$).
- (f) Dust grains can be locally heated up or destroyed in regions where $\text{H}\alpha$ emission is strong. We use this mask for the purpose of excluding the data points where $\text{H}\alpha \geq 10\text{ R}$.

Mask-(a) is applied to Figure 6, 7(c), 8, 9. Mask-(b), (c) are applied to the H I data, and mask-(d), (e), (f) to the dust data.

3.3. Velocity Structure

Figure 3(a) is a R.A.-velocity diagram of H I (image) and CO (contours, every 0.3 K from 0.3 K) in terms of Dec.-averaged intensities. Figure 3(b) shows the mean H I spectrum of this region. Although there is an intermediate-velocity component (intermediate-velocity cloud; IVC) at $V_{\text{LSR}} \lesssim -30\text{ km s}^{-1}$, its contribution to the column density is only up to $\sim 6\%$ of the total, we therefore use the data including all the velocity components.

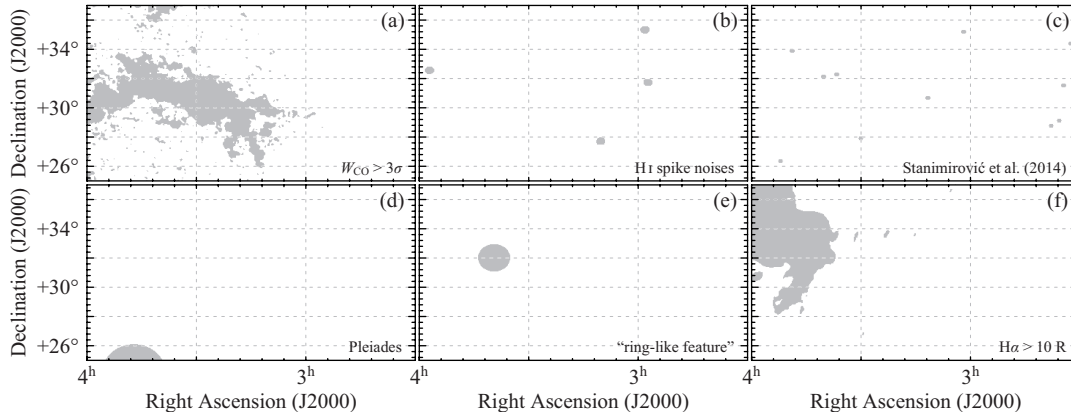


Figure 2. Mask maps used in the present study. We masked the data points (a) where $W_{\text{CO}} \geq 3\sigma$, (b) where spike noises are detected in HI spectra, (c) within an effective HPBW (8.4 arcmin) of background radio point sources described in Stanimirović et al. (2014), (d) within 1.5 deg of Pleiades, (e) within 56 arcmin from $(\alpha_{\text{J2000}}, \delta_{\text{J2000}}) = (3^{\text{h}} 39^{\text{m}} 30^{\text{s}}, +32^{\circ})$ (“ring-like feature” described in Lee et al. 2012), and (f) where $\text{H}\alpha \geq 10 \text{ R}$. (b) and (c) are applied to HI maps, (d), (e), and (f) are applied to dust maps.

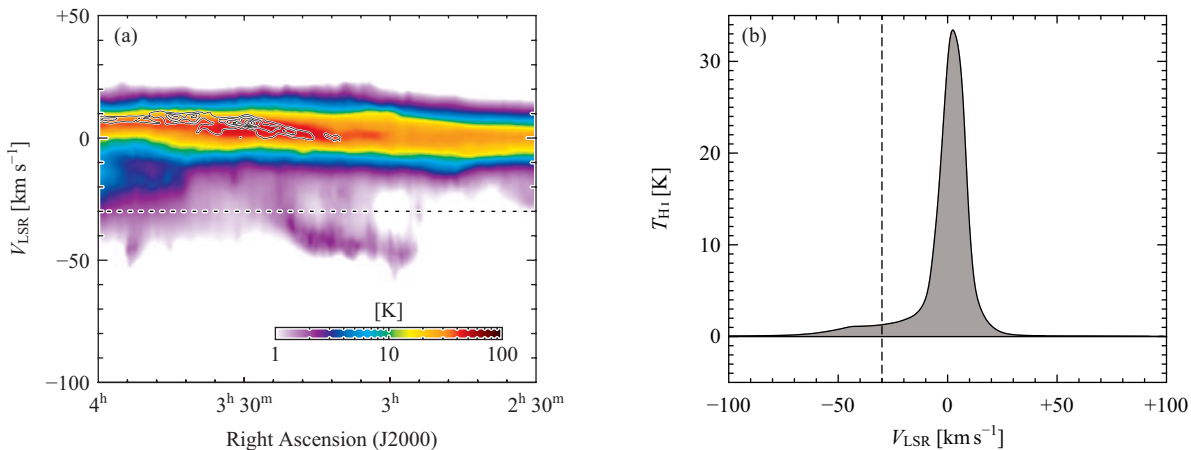


Figure 3. (a) A R.A.-velocity diagram of HI (image) and CO (contours) in terms of Dec.-averaged intensities. The contours are drawn every 0.3 K from 0.3 K. The average is calculated over the whole Dec. range shown in Figure (1). (b) An averaged HI spectrum calculated over the whole region shown in Figure (1) (b). The dashed lines indicate $V_{\text{LSR}} = -30 \text{ km s}^{-1}$.

3.4. Hydrogen Amount Estimation

Figure (4) is a double logarithmic correlation plot between A_J and τ_{353} . A linear regression in double logarithmic scale using the data of $A_J \geq 0.5 \text{ mag}$ and $\tau_{353} \geq 3 \times 10^{-5}$ yields the following relationship,

$$\tau_{353} = [(1.08 \pm 0.02) \times 10^{-4}] \times (A_J)^{1.32 \pm 0.04}. \quad (1)$$

We assume the uncertainties in the A_J data are 0.2 mag, which is the typical fluctuation nearby the Perseus cloud. Considering A_J as a linear tracer of N_{H} along each line of sight, Equation (1) indicates that dust emission cross section per hydrogen atom increases with the ~ 1.3 -th power of N_{H} . A similar analysis was done in Roy et al. (2013) for the Orion A region, and they concluded that the power index is 1.28. Our result is con-

sistent with it, and these results show dust evolution in high density regions. The grain size is typically up to $\sim 0.2 \mu\text{m}$ (Jones et al. 2013), which is much smaller than the J -band wavelength, $\sim 1.25 \mu\text{m}$. In addition, the grain size can change by only $\sim 0.02 \mu\text{m}$ (Ysard et al. 2015). Roy et al. (2013) and Forbrich et al. (2015) also argue that in the high density regions it is mostly the sub-millimeter opacity that is changing, not the infrared extinction. Therefore, changes in the grain size have small effect on the J -band extinction, and we can regard A_J as a linear tracer of N_{H} if DGR is uniform. In the present study, therefore, we adopted 1.3 as the power index (α) from Equation (1).

In Fukui et al. (2014, 2015) we suggested an algorithm for estimating the amount of the hydrogen gas using τ_{353}

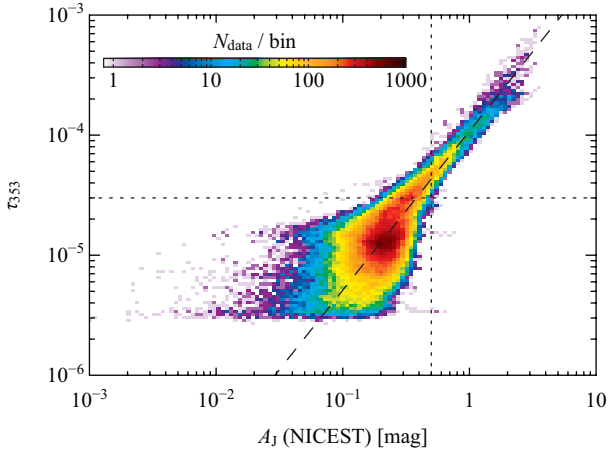


Figure 4. A double logarithmic scatter plot (density plot) between A_J and τ_{353} . Colors correspond to numbers of the data points included in each bin. The dashed line shows a relationship of $\tau_{353} = (1.08 \times 10^{-4}) \times (A_J)^{1.32}$, which is the result of a linear regression in double logarithmic scale using the data of $A_J \geq 0.5$ mag and $\tau_{353} \geq 3 \times 10^{-5}$. The dotted lines indicate $A_J = 0.5$ mag and $\tau_{353} = 3 \times 10^{-5}$.

as an accurate tracer of N_{H} . In Fukui et al. (2014) we assumed the relationship $\tau_{353} \propto N_{\text{H}}$. On the other hand, Fukui et al. (2015), considering the result of Roy et al. (2013), made discussion using the relationship of

$$\frac{\tau_{353}}{\tau_{353,\text{ref}}} = \left(\frac{N_{\text{H}}}{N_{\text{H},\text{ref}}} \right)^\alpha. \quad (2)$$

Here $\tau_{353,\text{ref}}$ and $N_{\text{H},\text{ref}}$ are normalization constants which satisfy the relationship of $N_{\text{H},\text{ref}} = (1.15 \times 10^8) \times X_{\text{HI}} \times \tau_{353,\text{ref}}$ (Fukui et al. 2015). In the present study we use Equation (2) by substituting $\alpha = 1.3$, $\tau_{353,\text{ref}} = 1.2 \times 10^{-6}$, and $N_{\text{H},\text{ref}} = 2.5 \times 10^{20} \text{ cm}^{-2}$;

$$\begin{aligned} N_{\text{H}} &= \left(\frac{\tau_{353}}{\tau_{353,\text{ref}}} \right)^{1/\alpha} N_{\text{H},\text{ref}} \\ &= (9.0 \times 10^{24}) \times (\tau_{353})^{1/1.3}. \end{aligned} \quad (3)$$

See Appendix A for the details of the determination of $\tau_{353,\text{ref}}$ and $N_{\text{H},\text{ref}}$.

Conventionally, the following equation is used to calculate the column number density of HI gas from an observable value, W_{HI} ,

$$N_{\text{HI}}^* \equiv X_{\text{HI}} \times W_{\text{HI}}. \quad (4)$$

Although widely used, this equation is obtained under the assumption that the HI gas is optically thin ($\tau_{\text{HI}} \ll 1$). The symbol N_{HI}^* is the HI column number density in the optically-thin limit. Therefore, when Equation (4) is used, the HI column number density can be underestimated if optically-thick HI gas exists. Here

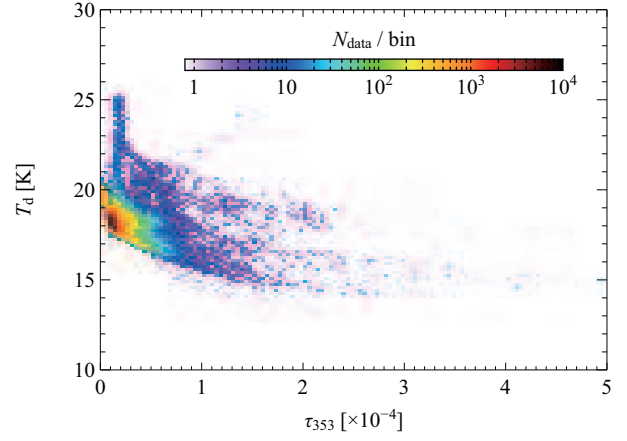


Figure 5. A scatter plot (density plot) between τ_{353} and T_{d} . It clearly shows a negative relationship as with Fukui et al. (2014) for MBM 53, 54, 55 region.

we will show that HI optical depth has significant effects on the estimation of the HI amount in the Perseus region.

Figure 5 is a scatter plot between τ_{353} and T_{d} of the region analyzed. As well as the MBM 53, 54, 55 region (Fukui et al. 2014), it clearly shows an anti-correlation relationship between the two quantities. As described in Section 3.1, dust grains are heated by interstellar radiation field (ISRF). In the areas where τ_{353} is small, the amount of ISM is also small and therefore the ISRF efficiently heats up the dust grains. Conversely, in the areas where τ_{353} is large, the amount of ISM is also large and the ISRF is shielded by the grains themselves, and they are cooled by dust radiation. The anti-correlation in Figure 5 reflects these picture. In addition, in the latter case, the dust growth can increase τ_{353} in such high density areas.

Figure 6 is a correlation plot between τ_{353} and W_{HI} colored by T_{d} in windows of 0.5 K intervals. Note that we applied the mask-(a) (CO mask) and therefore, $N_{\text{H}} = N_{\text{HI}}$ for the data points plotted in Figure 6. Although the correlation is not so good as a whole, the distributions of the data points on the τ_{353} - W_{HI} plane are clearly different when separated according to T_{d} . The scattering is small for the data points where T_{d} is high, and it becomes large with decreasing T_{d} . In particular, the distribution of the high- T_{d} points (such as $T_{\text{d}} > 19.5$ K) is elongated, and it seems to pass through the origin when it is extrapolated. On the other hand, the distribution of the low- T_{d} points is broadened along the τ_{353} axis. As we described above, this indicates that for such low- T_{d} points the amount of the ISM is large, and hence W_{HI} is saturated against τ_{353} because of the effect of large optical depth, i.e., $\tau_{\text{HI}} \gtrsim 0.3$. Therefore,

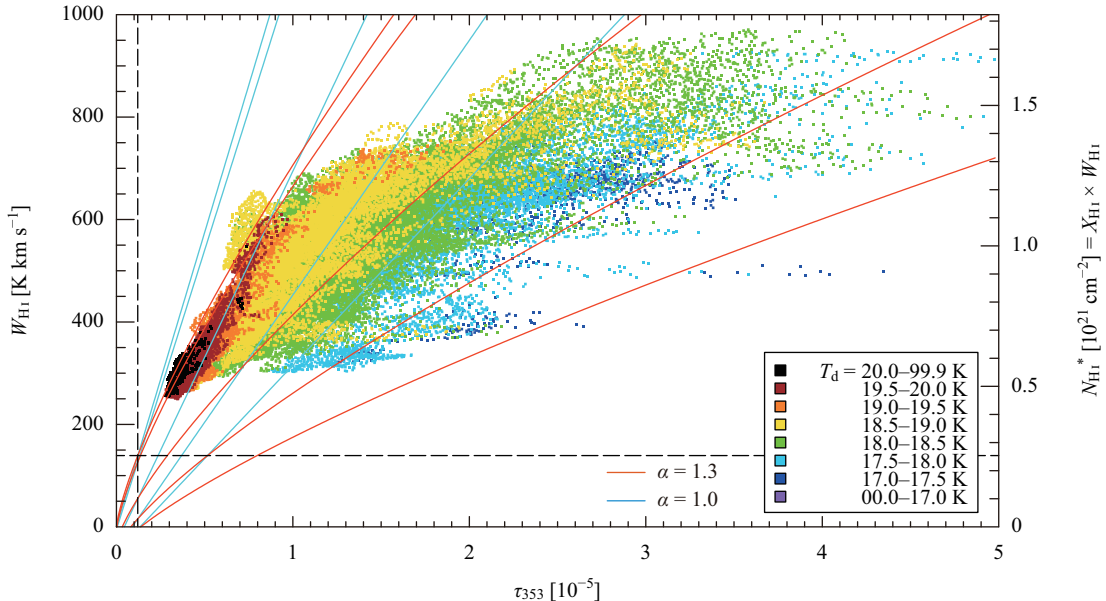


Figure 6. A scatter plot between τ_{353} and W_{HI} colored by T_d in 0.5 K windows. The right hand y -axis indicates the column number density of HI in the optically-thin limit (N_{HI}). The curves are theoretical relationships between both variables (Equation (7)) for the case of $\tau_{\text{HI}} = 0, 0.11, 1, 2, 3$ (from left to right). The light blue ones are for the case of $\alpha = 1.0$ and red ones for the case of $\alpha = 1.3$, respectively. We considered $T_{\text{bg}} = 3.7$ K and $\Delta V_{\text{HI}} = 13.7$ km s $^{-1}$ (mean values in this region) as constants. The dashed lines correspond to $\tau_{353,\text{ref}} = 1.2 \times 10^{-6}$ and $N_{\text{HI},\text{ref}} = 2.5 \times 10^{20}$ cm $^{-2}$ (Appendix A).

for such data points the amount of HI cannot be calculated by using Equation (4). It can be said that the reason of the low spatial correlation between τ_{353} and W_{HI} (Figure 1(b), (c)) is the effect of τ_{HI} . Note that there is another possibility to explain the bad correlation between τ_{353} and W_{HI} ; the presence of “CO-dark H $_2$ gas”, which is not detectable by the CO line. In Fukui et al. (2015), however, the authors examined the fraction of H $_2$ in the hydrogen gas by referring to the results of the UV measurements (Gillmon et al. 2006; Rachford et al. 2002), and found that the fraction is at most $\sim 10\%$. This means that HI dominates H $_2$ in the typical hydrogen gas. In addition, Fukui et al. (2012) revealed that the total hydrogen column number density ($N_{\text{HI}} + 2 N_{\text{H}_2}$) shows a good correlation with the TeV gamma ray distribution (a reliable tracer of the total hydrogen) in the supernova remnant RX J1713.7–3946 when the HI optical depth is corrected. From these, the bad correlation between τ_{353} and W_{HI} can be explained by optically-thick HI gas alone, without “CO-dark H $_2$ gas”. In the present study therefore, we did not consider “CO-dark H $_2$ gas”. The aspect of the W_{HI} saturation can be explained by using the radiation transfer equation as stated below.

The following Equations (5) and (6) are the radiation transfer equation of HI 21 cm line and the equation of HI optical depth, respectively, and both of them are derived theoretically (e.g., Draine 2011; Dickey & Lockman

1990).

$$W_{\text{HI}} = (T_s - T_{\text{bg}}) \Delta V_{\text{HI}} \{1 - \exp(-\tau_{\text{HI}})\} \quad (5)$$

$$\tau_{\text{HI}} = \frac{N_{\text{HI}}}{X_{\text{HI}}} \frac{1}{T_s} \frac{1}{\Delta V_{\text{HI}}} \quad (6)$$

These equations are independent of each other, and are valid regardless of whether τ_{HI} is negligible or not. We define ΔV_{HI} as $W_{\text{HI}}/T_{\text{HI}}(\text{peak})$, and τ_{HI} in Equations (5) and (6) are regarded as the average values over the velocity range ΔV_{HI} . From the two and Equation (3) we derive the following relationship;

$$W_{\text{HI}} = \left\{ \left(\frac{\tau_{353}}{\tau_{353,\text{ref}}} \right)^{1/\alpha} \frac{N_{\text{HI},\text{ref}}}{X_{\text{HI}}} \frac{1}{\tau_{\text{HI}}} \frac{1}{\Delta V_{\text{HI}}} - T_{\text{bg}} \right\} \times \Delta V_{\text{HI}} \{1 - \exp(-\tau_{\text{HI}})\}. \quad (7)$$

The lines/curves in Figure 6 show this relationships in cases of $\alpha = 1.0$ and 1.3 (light blue lines and red curves, respectively) when $\tau_{\text{HI}} \ll 1$, $\tau_{\text{HI}} = 0.11, 1, 2$, and 3 are substituted (from left to right). We applied $\Delta V_{\text{HI}} = 13.7$ km s $^{-1}$ and $T_{\text{bg}} = 3.7$ K, which are the mean values of the data points shown in Figure 6. The standard deviations of ΔV_{HI} and T_{bg} are 1.9 km s $^{-1}$ and 0.05 K, respectively. Note that $\tau_{\text{HI}} = 0.21$ is given in Appendix A. According to these curves, there is a trend that larger τ_{HI} gives a smaller slope, which is consistent with the distribution of the low- T_d points. Therefore, these equal- τ_{HI} curves should trace the distribution of the equal- T_d points. As shown in Figure 6, the curves

to which $\alpha = 1.3$ is applied show better correlations with the distributions of the data points rather than $\alpha = 1.0$ for both high- and low- T_d . This also suggests that it is important to take into account the dust evolution. We can say in addition that the small variances at high T_d (small τ_{HI}) suggest the uniform DGR and the uniform grain size.

Figure 7(a) is a spatial distribution of N_{H} calculated with Equation (3). Figure 7(b) shows a distribution of N_{HI}^* derived with Equation (4), which is the HI column number density at optically-thin limit. Note that in Figure 7(a) and (b) the scales of their color-bars are significantly different from each other. In Figure 7(c) we show a distribution of $N_{\text{H}}/N_{\text{HI}}^*$, which is the pixel-to-pixel ratio map of Figure 7(a) and (b). In this map, mask-(a) is applied in order to exclude the data points where H_2 can exist. We found that the mean value of $N_{\text{H}}/N_{\text{HI}}^*$ is ~ 1.8 (see also Figure 9), and hence in this region, the amount of HI is underestimated to be $\sim 57\%$ if Equation (4) is used. From these, it turns out that HI optical depth has a significant effect in estimating the amount of HI gas in the ISM.

Using Equation (3), we can estimate the total (atomic and molecular) amount of the hydrogen gas in a high accuracy without being affected by HI optical depth. However, note that Equation (3) alone cannot separate atomic and molecular components, and also cannot separate individual components located along the same line of sight.

3.5. τ_{HI} and T_s Estimation

Once N_{H} is derived with Equation (3), τ_{HI} and T_s can be calculated independently as solutions of a system of equations (5) and (6) (Fukui et al. 2014, 2015). Since the solutions of the coupled equations cannot be expressed analytically, they are numerically calculated. We note that in the limit of $\tau_{\text{HI}} \ll 1$ the solutions are indeterminate. Figure 8 shows the spatial distributions of (a) τ_{HI} and (b) T_s , respectively. In order to compare with the result of τ_{HI} obtained based on HI absorption measurements in Stanimirović et al. (2014), we spatially interpolated (bilinear method) the HI spectra masked by mask-(c) and calculated the solutions.

In Figure 9 we show mass-weighted histograms of (a) N_{H} , (b) $N_{\text{H}}/N_{\text{HI}}^*$, (c) τ_{HI} , and (d) T_s , respectively, for the region shown in Figure 8. We assumed the distance to the Perseus cloud as 300 pc (Bally et al. 2008), and the mass is calculated by including hydrogen and helium. We found the mass-weighted mean values as $\langle N_{\text{H}} \rangle \sim 1.7 \times 10^{21} \text{ cm}^{-2}$, $\langle N_{\text{H}}/N_{\text{HI}}^* \rangle \sim 1.6$, $\langle \tau_{\text{HI}} \rangle \sim 0.92$, and $\langle T_s \rangle \sim 97 \text{ K}$. The ratio of the HI mass with $\tau_{\text{HI}} < 1$ is $\sim 37\%$ of the total mass and as shown in Figure 6

optically thick HI cannot be ignored. In Fukui et al. (2014) we found that $\langle T_s \rangle \sim 30 \text{ K}$ around the MBM 53, 54, 55/HLCG 92–35 clouds, which is somewhat lower than that for the Perseus region. It is possible that the Perseus cloud is located in the Gould’s belt, which contains heat sources including some SFRs and OB associations.

Figure 10 shows examples of the τ_{HI} and T_s solutions. The curves of Equation (5) (blue) and Equation (6) (red), and the solutions of τ_{HI} and T_s (purple) are drawn on the $\tau_{\text{HI}}-T_s$ plane. We show the solutions toward the background radio sources described in Stanimirović et al. (2014). As described above, the HI spectra toward the directions are spatially interpolated. The blue and red dashed curves indicate 1σ uncertainties for each curve, and we defined the uncertainties in the solutions (purple lines) as the intersections of the dashed curves. Table 2 is the results of the calculations. For each data point the solutions of τ_{HI} and T_s are well determined.

3.6. X_{CO} estimation

The X_{CO} factor, which is an empirical conversion factor, has been used in order to estimate H_2 column number density (N_{H_2}) from the velocity-integrated intensity of the CO line (W_{CO}). Conventionally, $X_{\text{CO}} \sim (1-2) \times 10^{20} \text{ cm}^{-2} \text{ K}^{-1} \text{ km}^{-1} \text{ s}$ is assumed as a typical value for the Galaxy (e.g., Bolatto et al. 2013). Here, since N_{H} is obtained with a higher accuracy, we are able to determine X_{CO} by using the *Planck* data and W_{CO} data.

Figure 11 indicates correlation plots between W_{CO} (x -axis) and N_{H} (y -axis). Fitting the distribution of the data points and calculating the slope and the intercept, we can separate the atomic component and the molecular component from N_{H} .

$$\begin{aligned} N_{\text{H}} &= N_{\text{HI}} + 2 N_{\text{H}_2} \\ N_{\text{H}_2} &= X_{\text{CO}} \times W_{\text{CO}} \end{aligned}$$

So, we obtain the following,

$$\begin{aligned} N_{\text{H}} &= (2 X_{\text{CO}}) W_{\text{CO}} + N_{\text{HI}} \\ &\equiv (\text{slope}) \times W_{\text{CO}} + (\text{intercept}). \end{aligned} \quad (8)$$

The intercept gives the atomic component, and the slope gives the molecular component and the X_{CO} factor (= slope/2). Note that the contribution of the atomic component is a mean value, and we assumed that it is constant against W_{CO} . We used an outlier-robust linear regression method in order to avoid the effect due to the data points where W_{CO} is saturated against N_{H} . For this purpose, we utilized the ROBUST_LINEFIT routine provided in The IDL Astronomy User’s Library

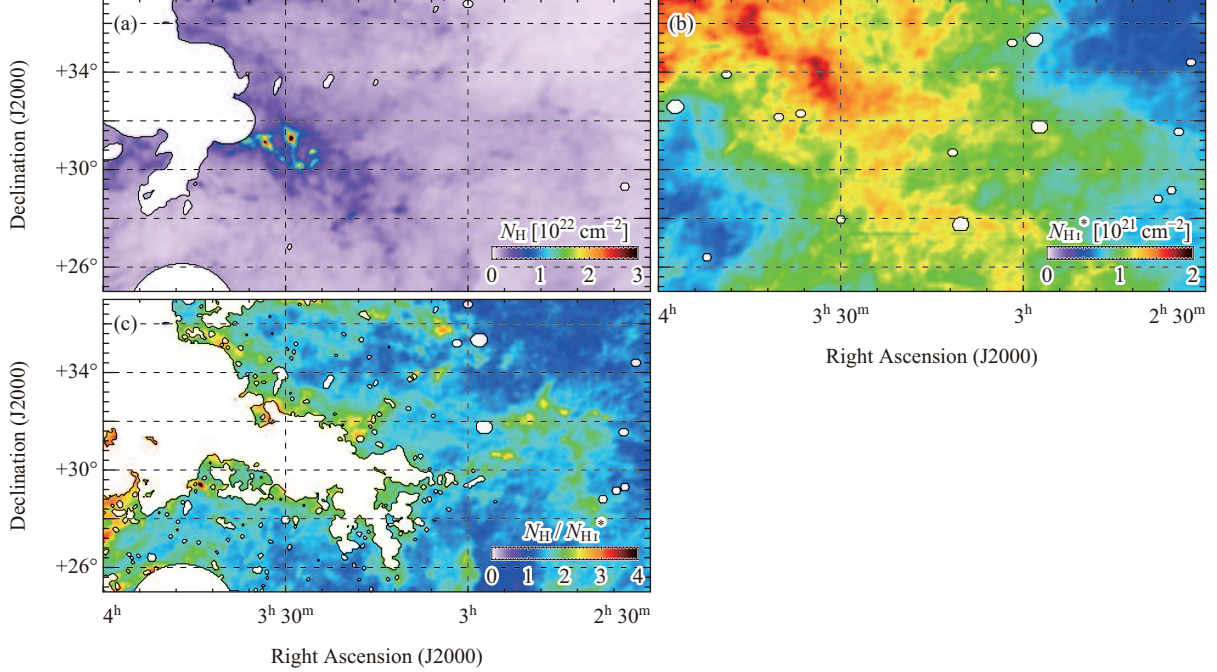


Figure 7. (a) A map of N_{H} calculated by Equation (3). Masks-(d), (e), (f) are applied. (b) A spatial distribution of HI column density calculated under the assumption of the optically thin limit, $N_{\text{HI}}^* (= X_{\text{HI}} \times W_{\text{HI}})$. Masks-(b), (c) are applied. (c) A pixel-to-pixel ratio map between (a) and (b) ($N_{\text{H}}/N_{\text{HI}}^*$). We found the mean value as $\langle N_{\text{H}}/N_{\text{HI}}^* \rangle \sim 1.6$. Mask-(a) is applied in addition.

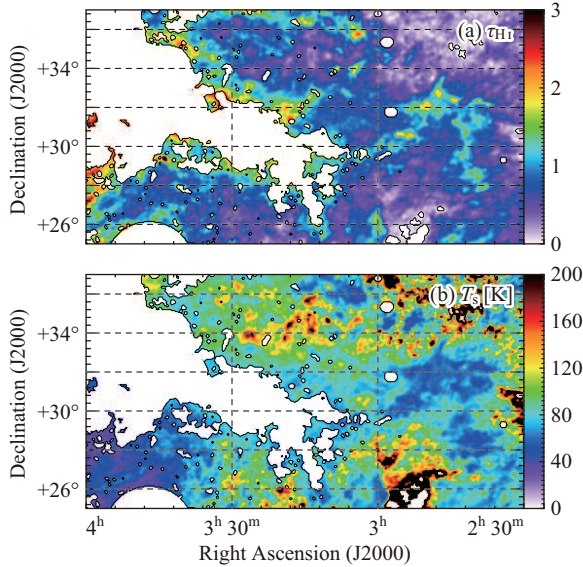


Figure 8. Estimated spatial distributions of (a) τ_{HI} and (b) T_s , which are the solutions of the system of equations (5) and (6). For the purpose of comparisons with the results of Stanimirović et al. (2014), we spatially interpolated the HI spectra toward the background sources using the bilinear interpolation method and computed τ_{HI} and T_s .

(Landsman 1993). In the present study, we estimated the spatial distribution of the X_{CO} factor by the procedure described below.

1. We prepare a “window”, which extracts the data points within a 1-degree radius from a certain point. This radius is determined in order to ensure a sufficient number of data points to be fitted.
2. By using the data points inside the window, we estimate the X_{CO} factor from the $W_{\text{CO}}-N_{\text{H}}$ plot.
3. We regard the resulting X_{CO} as the value of the center point of the window.
4. The X_{CO} map can be obtained by iteratively calculating the X_{CO} factor for all the data points while moving the center of the window pixel by pixel (this process is similar to image convolution).

Figure 12(a) and (b) shows the map of W_{CO} and N_{H} (already shown in Figure 1(a) and Figure 7(a)), but only Mask-(d) and (e) are applied in order to compare with previous studies (Lee et al. 2012, 2014, described below). The four overlaid circles (A)–(D) indicate the examples of the “window”, corresponding to the panels (a)–(d) of Figure 11, respectively. The resulting X_{CO} map is shown in Figure 12(c). We found the X_{CO} factor significantly varies within the Perseus cloud, $X_{\text{CO}} \sim (0.3\text{--}2.0) \times 10^{20} \text{ cm}^{-2} \text{ K}^{-1} \text{ km}^{-1} \text{ s}$ with a typical uncertainty of 10–50%. The X_{CO} variation within molecular clouds is discussed in some previous studies (e.g., Magnani et al. 1998; Cotten & Magnani

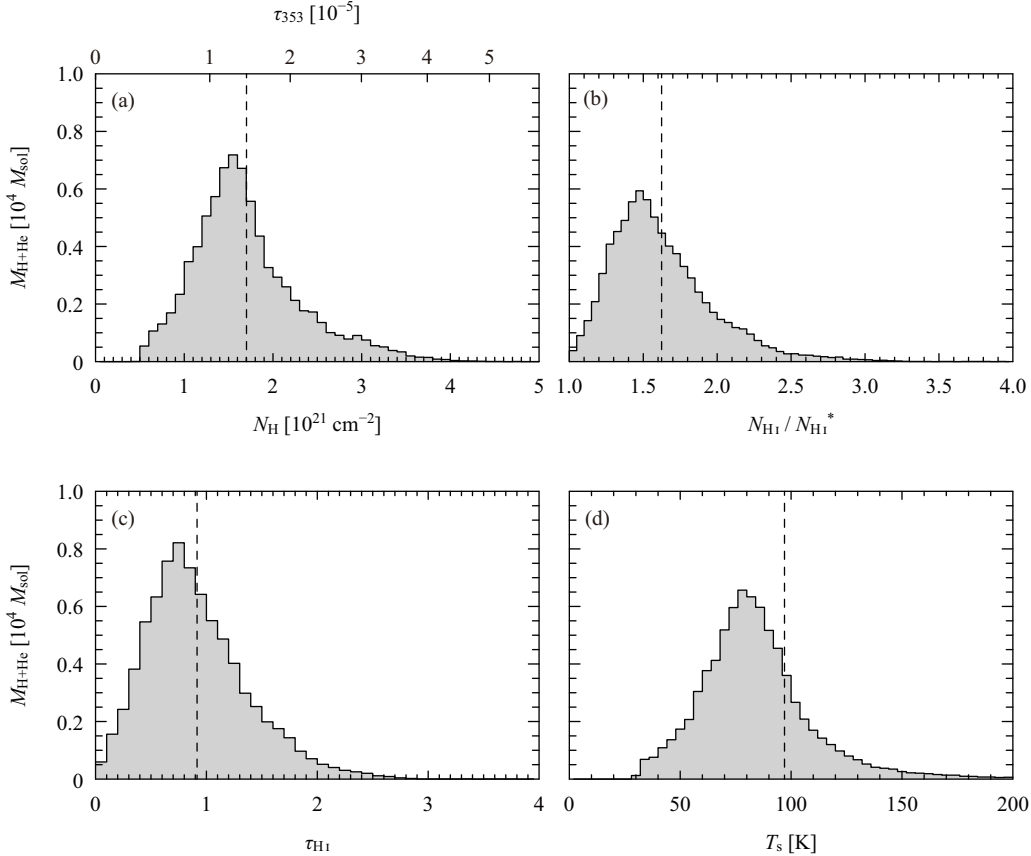


Figure 9. Mass-weighted histograms of (a) N_{H} , (b) $N_{\text{HI}}/N_{\text{HI}}^*$, (c) τ_{HI} , and (d) T_s for the region shown in Figure (8). We assume a distance of 300 pc and the mass includes helium. The dashed lines indicate the mass-weighted mean values of each histogram. In panel (a) the upper x-axis shows the τ_{353} calculated by using Equation (3).

2013; Lee et al. 2014), and the present result agrees with these results. We also found the average value is $\langle X_{\text{CO}} \rangle \sim 1.0 \times 10^{20} \text{ cm}^{-2} \text{ K}^{-1} \text{ km}^{-1} \text{ s}$ (Figure 11(e)), which is consistent with the empirical and typical value of the Galaxy, $(1-2) \times 10^{20} \text{ cm}^{-2} \text{ K}^{-1} \text{ km}^{-1} \text{ s}$. On the other hand, Lee et al. (2012, 2014) also estimated a spatial distribution the X_{CO} factor in the Perseus molecular cloud. However, they obtained the average value of $\langle X_{\text{CO}} \rangle \sim 0.3 \times 10^{20} \text{ cm}^{-2} \text{ K}^{-1} \text{ km}^{-1} \text{ s}$, which is $\sim 1/3$ of our result. We will explain this discrepancy between these two results on the X_{CO} factor in the next section.

4. DISCUSSIONS

4.1. X_{CO}

As mentioned above, Lee et al. (2012, 2014) also estimated the spatial distribution of the X_{CO} factor in the Perseus molecular cloud. Their procedure for the X_{CO} estimation is briefly described below:

1. N_{H} is estimated by using A_V as a tracer of the total amount of hydrogen. They used the dust-to-

gas ratio (DGR) as the conversion factor,

$$N_{\text{H}} = \frac{A_V}{\text{DGR}}, \quad \text{DGR} = 1.1 \times 10^{-21} \text{ mag}^{-1} \text{ cm}^2.$$

2. N_{H_2} is calculated by subtracting N_{HI} from N_{H} ,

$$N_{\text{H}_2} = \frac{1}{2}(N_{\text{H}} - N_{\text{HI}}). \quad (9)$$

Note that in Lee et al. (2012, 2014) $\tau_{\text{HI}} = 0$ is assumed, that is, $N_{\text{HI}} = N_{\text{HI}}^*$ is assumed.

3. The resulting X_{CO} map is obtained by dividing N_{H_2} by W_{CO} for each data point.

The available A_V map (“COMPLETE survey” (Lombardi & Alves 2001) based on the 2MASS data), however, covers only the central region of the cloud, hence they made a wide-area “simulated” A_V map by using *IRAS* data:

1. The wide-area dust temperature map was estimated from the ratio of the intensities of the IRIS 60, 100 μm maps. Effect from Very Small Grains (VSGs) was considered for the IRIS 60 μm map.

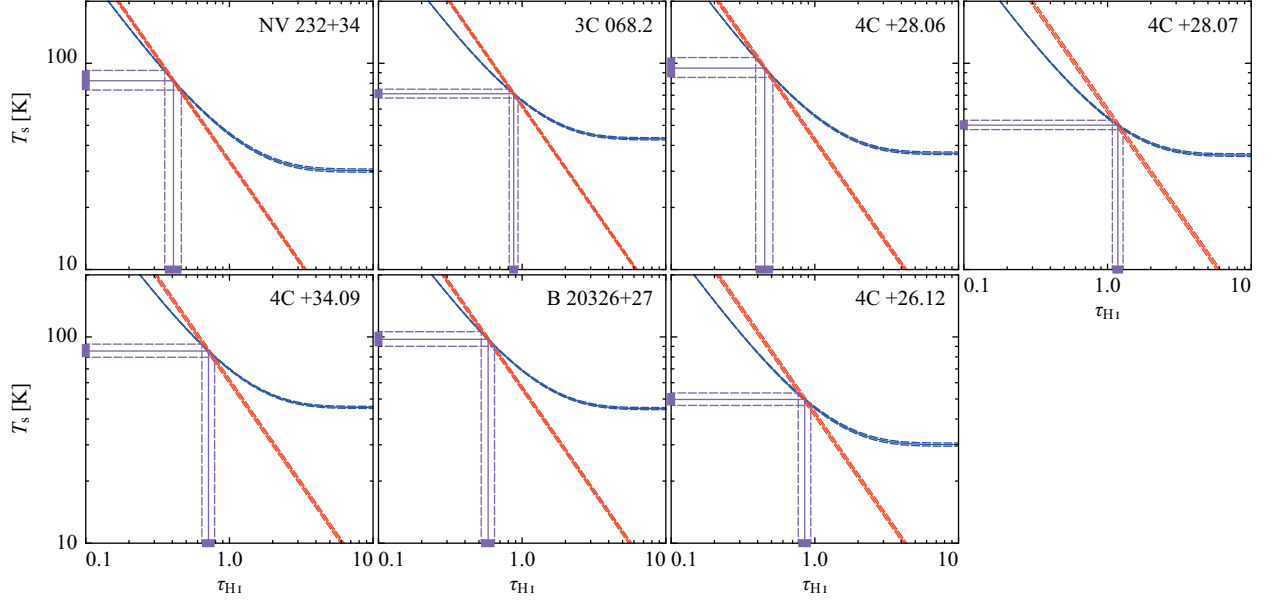


Figure 10. Examples of the τ_{HI} and T_s estimations. As examples we show the results toward background radio sources described in Stanimirović et al. (2014). Blue solid lines are calculated by Equation (5) and red ones by Equation (6). The solutions of τ_{HI} and T_s (purple solid lines) are obtained in terms of the intersections of the red and blue lines. Dashed lines indicate the uncertainty ranges for each solid line.

Table 2. List of radio continuum sources in Table 1 of Stanimirović et al. (2014)

Name	Position		τ_{353} [10^{-5}]	N_{H} [10^{21} cm^{-2}]	present study			Stanimirović et al. (2014)
	α_{J2000}	δ_{J2000}			T_s [K]	τ_{HI}	$\tau_{\text{HI}} \times \Delta V_{\text{HI}}$ [km s^{-1}]	$\int \tau_{\text{HI}} dV$ [km s^{-1}]
(a)	(b)	(c)	(d)	(e)	(f)	(g)	(h)	(i)
NV 0232+34	2 ^h 32 ^m 28 ^s .72	+34° 24 ^m 06 ^s .08	0.5	0.8	82 ⁺¹⁰ ₋₈	0.4±0.1	5.1±0.7	1.89±0.14
3C 068.2	2 ^h 34 ^m 23 ^s .87	+31° 34 ^m 17 ^s .62	0.9	1.2	71 ⁺⁴ ₋₃	0.9±0.1	9.0±0.6	4.77±0.14
4C +28.06	2 ^h 35 ^m 35 ^s .41	+29° 08 ^m 57 ^s .73	0.7	1.0	95 ⁺¹² ₋₉	0.4±0.1	5.8±0.8	3.67±0.04
4C +28.07	2 ^h 37 ^m 52 ^s .42	+28° 48 ^m 09 ^s .16	1.1	1.4	50 ⁻³ ₋₂	1.2±0.1	15.7 ^{+1.4} _{-1.3}	4.43±0.15
4C +34.09	3 ^h 01 ^m 42 ^s .38	+35° 12 ^m 20 ^s .84	1.1	1.4	85 ⁺⁷ ₋₆	0.7±0.1	8.9±0.9	4.05±0.04
4C +30.04	3 ^h 11 ^m 35 ^s .19	+30° 43 ^m 20 ^s .62	2.0	2.2	7.62±0.08
B 20326+27	3 ^h 29 ^m 57 ^s .69	+27° 56 ^m 15 ^s .64	1.2	1.4	97 ⁺⁹ ₋₇	0.6±0.1	8.1±0.9	4.50±0.04
3C 092	3 ^h 40 ^m 08 ^s .55	+32° 09 ^m 02 ^s .32	8.1	6.5	13.96±0.99
3C 093.1	3 ^h 48 ^m 46 ^s .93	+33° 53 ^m 15 ^s .41	2.2	2.4	8.93±0.23
4C +26.12	3 ^h 52 ^m 04 ^s .36	+26° 24 ^m 18 ^s .11	0.8	1.1	50 ⁺⁴ ₋₃	0.9±0.1	11.7 ^{+1.2} _{-1.1}	4.87±0.04

NOTE— (a), (b), and (c): Names and coordinates of the radio continuum sources listed in Table 1 of Stanimirović et al. (2014). (d): τ_{353} values toward the sources. (e): N_{H} values toward the sources calculated by Equation (3). (f) and (g): HI spin temperature and HI optical depth calculated by Equations (5) and (6). (h): Velocity-integrated HI optical depth derived from column (g) and ΔV_{HI} . (i): Total Velocity-integrated HI optical depth derived from the Gaussian parameters of τ_{HI} spectra of Stanimirović et al. (2014).

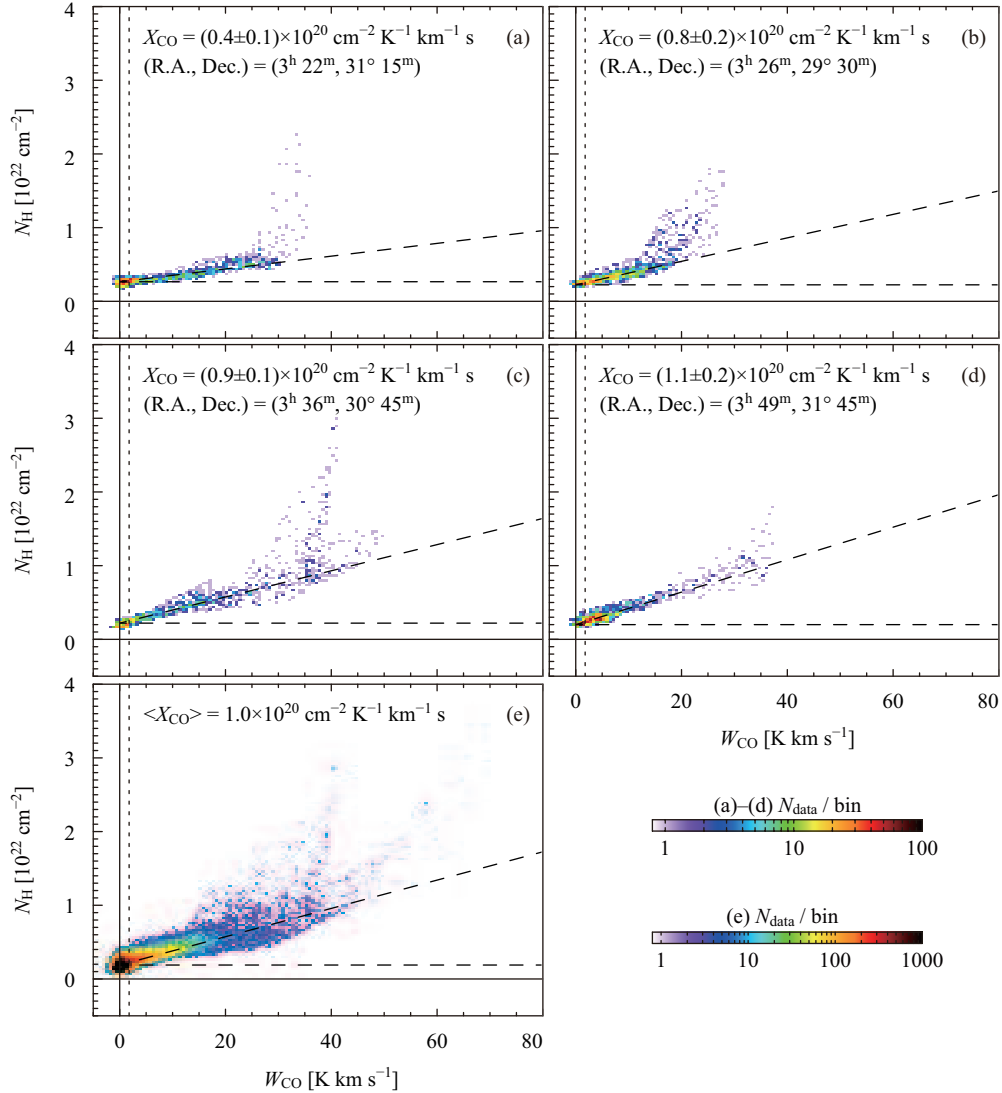


Figure 11. (a)–(d) Examples of $W_{\text{CO}}-N_{\text{H}}$ correlation plots (density plots) using the data points inside the $r = 1$ deg windows (A)–(D) shown in Figure 12. (e) The same as panels (a)–(d) but using the all data points shown in Figure 12(a) and (b). The outlier-robust linear regression method is used to fit the data in order to avoid effects due to saturated points. The data points of $W_{\text{CO}} \geq 3\sigma$ are used. The dotted lines indicate $W_{\text{CO}} = 3\sigma$. The dashed lines show the resulting slopes and intercepts of the regressions, and X_{CO} is estimated by Equation (8) by using these slopes. The average value of X_{CO} is calculated as $\langle X_{\text{CO}} \rangle \sim 1.0 \times 10^{20} \text{ cm}^{-2} \text{ K}^{-1} \text{ km}^{-1} \text{ s}$ from panel (e).

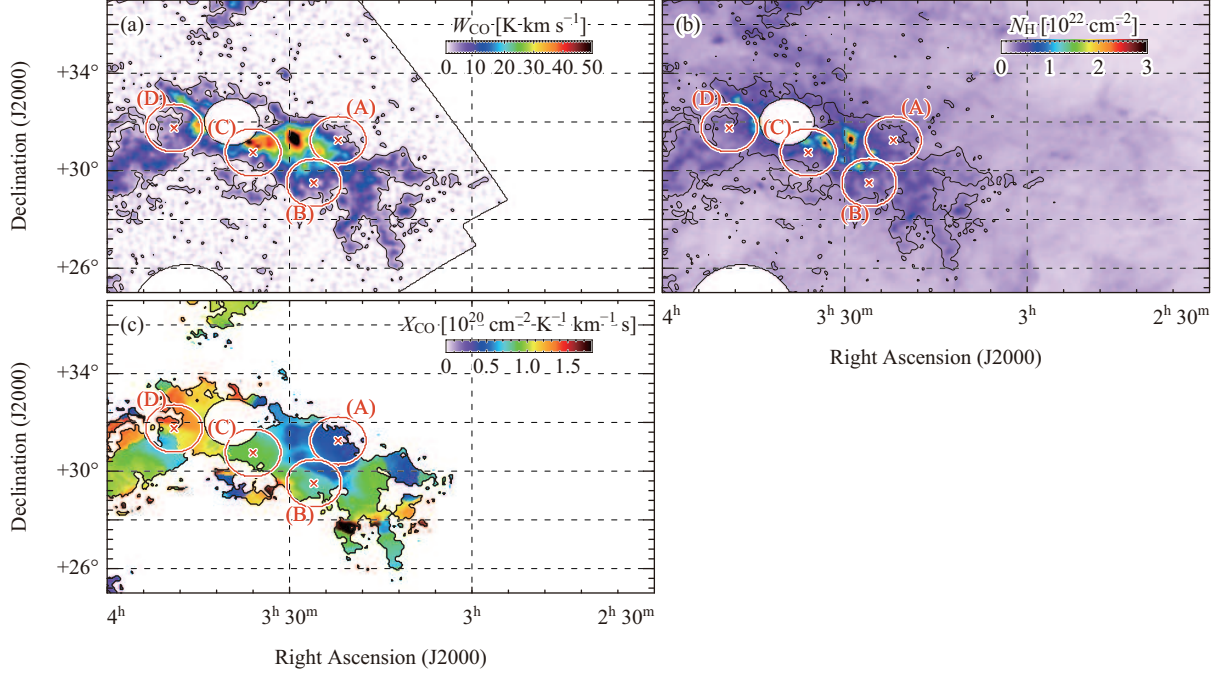


Figure 12. (a) The map of W_{CO} overlaid with $r = 1^\circ$ windows (A)–(D). (b) The map of N_{H} overlaid with the windows (A)–(D). (c) A map of the estimated spatial distribution of X_{CO} factor. In Figure 11(a)–(d) we show examples of $W_{\text{CO}}-N_{\text{H}}$ correlation plots using the data points inside the windows (A)–(D) used to compute X_{CO} at their center positions (X-points). The average value of X_{CO} is $\langle X_{\text{CO}} \rangle = 1.0 \times 10^{20} \text{ cm}^{-2} \text{ K}^{-1} \text{ km}^{-1} \text{ s}$ (Figure 11(e)).

2. The wide-area map of optical depth at $100 \mu\text{m}$ (τ_{100}) was derived from the ratio of the IRIS $100 \mu\text{m}$ map to the intensity at $100 \mu\text{m}$ of the blackbody radiation at derived dust temperature. The zero point offset in τ_{100} was also corrected.
3. The wide-area “simulated” A_V map was obtained from the τ_{100} map by using the conversion factor obtained by the correlation between τ_{100} and the COMPLETE A_V map.

Figure 13(a) shows histograms of X_{CO} derived in Section 3.6 and X_{CO} reproduced by the same procedure as Lee et al. (2012, 2014). Note that the data points used are the same as Figure 12, not the same as Lee et al. (2012, 2014). The average values are $\langle X_{\text{CO}} \rangle \sim 1.0 \times 10^{20} \text{ cm}^{-2} \text{ K}^{-1} \text{ km}^{-1} \text{ s}$ and $\langle X_{\text{CO}} \rangle_{\text{Lee}} \sim 4.0 \times 10^{19} \text{ cm}^{-2} \text{ K}^{-1} \text{ km}^{-1} \text{ s}$ for the present study and

the Lee’s result, respectively, and the result of Lee et al. (2012, 2014) is well reproduced. In Figure 13(b) we show histograms of N_{H} derived by using Equation (3) and the same method as Lee et al. (2012). We found $\langle N_{\text{H}} \rangle \sim 4.3 \times 10^{21} \text{ cm}^{-2}$ and $\langle N_{\text{H}} \rangle_{\text{Lee}} \sim 1.4 \times 10^{21} \text{ cm}^{-2}$, hence Lee et al. (2012) underestimated N_{H} to be $\sim 40\%$.

Here, we will quantitatively examine the difference in X_{CO} between the present study and Lee et al. (2012, 2014). Since $X_{\text{CO}} = N_{\text{H}_2}/W_{\text{CO}}$, the underestimation of X_{CO} in Lee et al. (2012, 2014) is caused by the underestimation of N_{H_2} in Equation (9). Therefore, we investigated the cause of the underestimation of N_{H} and N_{H_1} in Equation (9). Figure 14(a) is a correlation plot between τ_{353} and I_{100} . The correlation coefficient is ~ 0.5 and we found that I_{100} is not a good tracer of N_{H} . Figure 14(b) shows a correlation between N_{H} calculated by Equation (3) and N_{H} calculated by the same method as

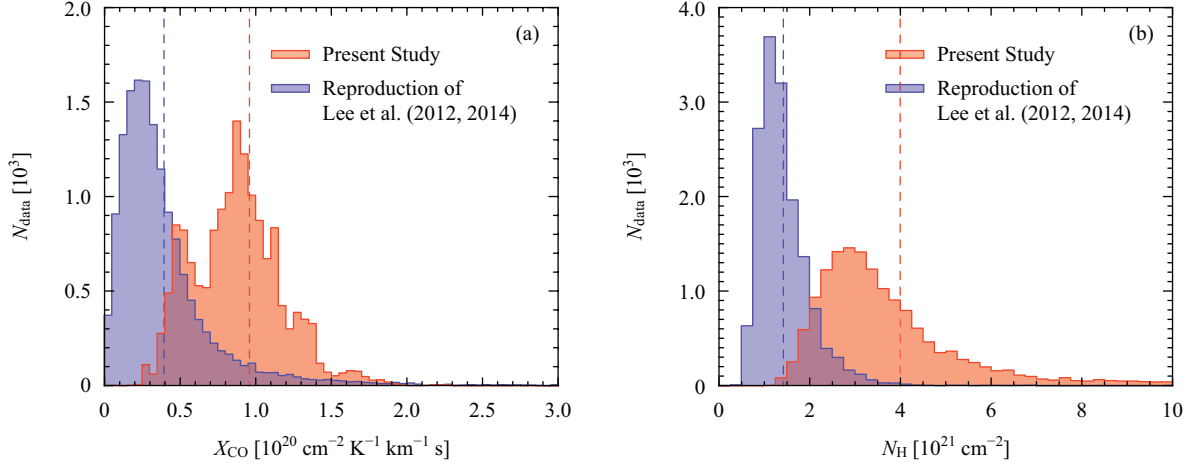


Figure 13. Histograms of (a) X_{CO} and (b) N_{HI} for the region shown in Figure (12). The orange ones are obtained in the present study and purple ones are obtained by replicating the procedures described in Lee et al. (2012, 2014). The dashed lines denote the average values of each histogram.

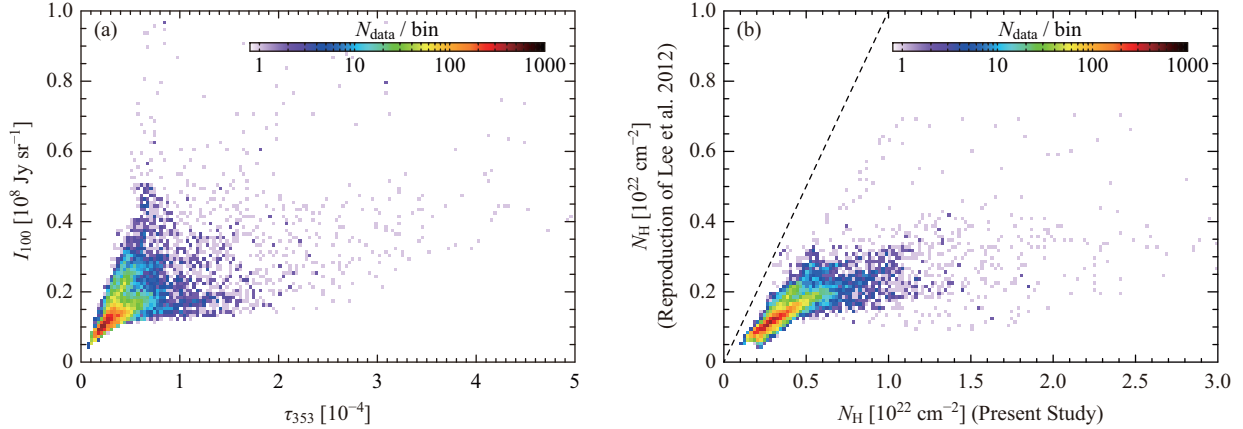


Figure 14. Correlation plots (density plots) between (a) τ_{353} and I_{100} , (b) N_{HI} calculated by Equation (3) and N_{HI} calculated by the same method as Lee et al. (2012). The dashed line in panel (b) indicates the 1:1 relationship.

Lee et al. (2012). The dashed line indicates the 1:1 relationship. The latter is clearly underestimated ($\sim 35\%$ on average) against the former. Separately from that, in Lee et al. (2012, 2014) the effect of HI optical depth was not considered. As shown in Section 3.4 the effect of τ_{HI} is $N_{\text{HI}}/N_{\text{HI}}^* \sim 1.6$. Therefore, N_{HI} is underestimated to be (at least) $\sim 62\%$ on average. In addition, the integrated velocity range of HI spectra is from -5 km s^{-1} to $+15 \text{ km s}^{-1}$ in Lee et al. (2012). This corresponds to $\sim 76\%$ of the total integrated intensity of the mean spectrum shown in Figure 3(b). From these, N_{HI} in Equation (9) is underestimated at least $62\% \times 76\% \sim 50\%$ or less on average. In Lee et al. (2012, 2014), the right-hand side of Equation (9) is underestimated to be $\sim 40\%$, and hence, X_{CO} is underestimated to be $\sim 40\%$ against our result.

Figure 15 shows a correlation between W_{CO} and X_{CO} maps. We spatially smoothed the W_{CO} map to a 1 deg

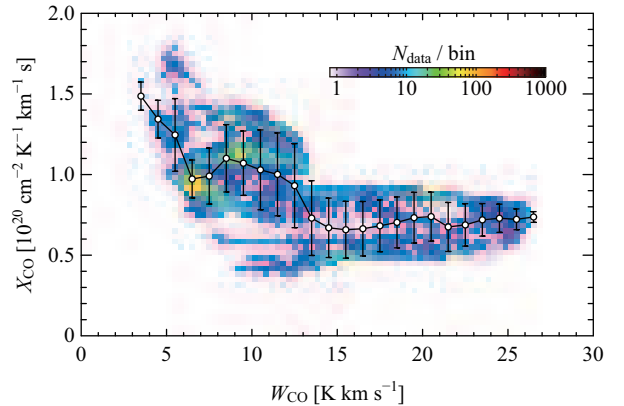


Figure 15. A correlation plot (density plot) between W_{CO} and X_{CO} . In order to compare with X_{CO} , we spatially smoothed the W_{CO} map to a 1 deg effective HPBW. The white circles and the vertical bars indicate the average and the standard deviation of X_{CO} in each 1 K km s^{-1} bin.

effective HPBW in order to compare with X_{CO} , and we plotted the data points where $X_{\text{CO}} \geq 3\sigma$. We also show the average and the standard deviation of X_{CO} in each 1 K km s^{-1} bin as the white circles and the vertical bars. From this plot, we found an anti-correlation relationship between the two variables. This anti-correlation reflects that in the diffuse (low- W_{CO}) region CO molecule is photo-dissociated more effectively than H_2 , and therefore X_{CO} increases. This trend is consistent with the result in Cotten & Magnani (2013); Schultheis et al. (2014), and we can say that the spatial distribution of X_{CO} can be well calculated by using the present method.

4.2. Mass

The total mass of the hydrogen gas including H I , H_2 , and helium is derived as $M_{\text{H}} = 1.8 \times 10^5 M_{\odot}$ by using N_{H} calculated by Equation (3). We assumed the distance to the Perseus cloud as 300 pc (Bally et al. 2008). On the other hand, the mass of the molecular hydrogen gas is calculated as $M_{\text{H}_2} = 2.5 \times 10^4 M_{\odot}$ by using W_{CO} and the X_{CO} map obtained in Section 3.6. From these masses, we calculate the mass of the atomic hydrogen gas as $M_{\text{H I}} = M_{\text{H}} - M_{\text{H}_2} = 1.5 \times 10^5 M_{\odot}$. This indicates that the molecular cloud is surrounded by the atomic gas whose mass is by an order of magnitude larger than that of the molecular one, and it also indicates that the atomic gas is the most principal component of the ISM. This is consistent with the result for the MBM 53, 54, 55/HLCG 92–35 region described in Fukui et al. (2014). Note that the virial mass of the H I gas around the Perseus cloud is calculated as $\sim 2 \times 10^6 M_{\odot}$ if we assume that the gas around the Perseus cloud is a sphere with a radius of 50 pc and a velocity width of 15 km s^{-1} . This is an order of magnitude larger than the estimated mass above ($1.5 \times 10^5 M_{\odot}$), and hence, it is not gravitationally bound. The virial mass of the CO cloud is $\sim 1 \times 10^5 M_{\odot}$ if we assume that its radius is 25 pc and its velocity width is 5 km s^{-1} . The molecular mass estimated above ($2.5 \times 10^4 M_{\odot}$) is $\sim 1/4$ of this virial mass, and the cloud traced by $^{12}\text{CO}(J=1-0)$ line is also not gravitationally bound. Since the molecular cloud is denser than the atomic cloud, the mass of the molecular cloud is relatively closer to its virial mass than that of the atomic cloud.

4.3. $\tau_{\text{H I}}$

As one of the previous studies on the atomic gas in the Perseus region, Stanimirović et al. (2014) calculated the H I optical depth toward 26 extra-Galactic radio continuum sources (such as quasars). They calculated $\tau_{\text{H I}}$ as a function of velocity toward each radio source by using the method described in Heiles & Troland (2003).

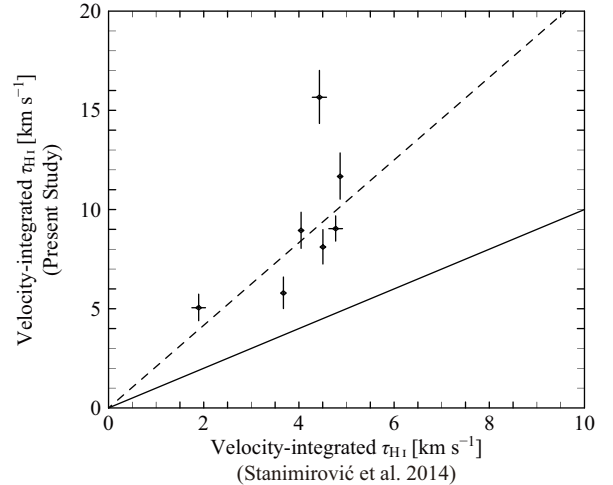


Figure 16. A correlation plot between velocity-integrated values of $\tau_{\text{H I}}$ derived in Stanimirović et al. (2014) (x -axis) and $\tau_{\text{H I}} \times \Delta V_{\text{H I}}$ derived in the present study (y -axis). The solid line indicates the 1:1 relationship between both variables. The dashed line is the result of a linear regression through the origin. Its slope is 2.1.

The calculated $\tau_{\text{H I}}$ spectra were fitted with a sum of Gaussian functions, and the peak $\tau_{\text{H I}}$ values and the Gaussian FWHMs (full width at half maximum) of each velocity component were derived. However, they found the optically-thick H I gas only toward $\sim 15\%$ of lines of sight. We test the results in Stanimirović et al. (2014) and Fukui et al. (2014, 2015), which differ a factor of several. To do this, we compare $\tau_{\text{H I}}$ derived in Stanimirović et al. (2014) and that obtained in Section 3.5. Since our $\tau_{\text{H I}}$ corresponds to the average value within given velocity width ($\Delta V_{\text{H I}}$) (see Section 3.4) we compare the following two values toward each radio source located in the region we analyzed; (1) the sum of the areas of each Gaussian component of the $\tau_{\text{H I}}$ profiles calculated in Stanimirović et al. (2014), and (2) the products of our $\tau_{\text{H I}}$ and $\Delta V_{\text{H I}}$. The results are listed in the column 8 and 9 of Table 2. Note that 4C +30.04, 3C 092, and 3C 093.1 are located at the masked area, therefore $\tau_{\text{H I}}$ cannot be calculated by our method toward them. Although there is a rough positive correlation between them, they differ 2–4 times as a concrete numerical value. The correlation between them is plotted in Figure 16. The solid line indicates the one-to-one relationship (slope = 1), and the dashed line is the best-fit regression line through the origin (slope = 2.1). The results in Stanimirović et al. (2014) are systematically smaller than our results, and it is obvious that there is a discrepancy between these two results. This discrepancy can, however, be explained by characteristics of the data used to derive $\tau_{\text{H I}}$ in the present study and Stanimirović et al. (2014).

In Stanimirović et al. (2014) τ_{HI} is calculated based on the 21 cm absorption spectrum toward the extra-Galactic point sources. Since these point sources have infinitesimal apparent size, the absorption by the HI gas actually occurs toward the very direction of each source. However, Inoue & Inutsuka (2012) and McClure-Griffiths et al. (2006) revealed that the cold neutral medium (CNM), which is an optically-thick component of the HI gas, has highly filamentary and spatially inhomogeneous structure. Based on the three-dimensional numerical simulation of magnetohydrodynamics (MHD) (Inoue & Inutsuka 2012), we found that the CNM accounts for typically $\sim 30\%$ of the 2D-projected area (Fukui et al. 2017). Hence, the probability with which the CNM affects the absorption toward the point sources is small. Therefore, unless the observational beam size is not infinitesimal, absorption measurements tend to detect only warm neutral medium (WNM) and tend to regard the optical depth of the WNM as the average value within the beam. On the other hand, we use the emission data of gas and dust, and they include information from both the CNM and the WNM within the large beam ($\gtrsim 4$ arcmin). Therefore, we can say that the discrepancy of τ_{HI} is due to the difference between the measurement methods (absorption toward point sources or emission). We independently confirm this result by using the numerical simulation (“synthetic” observations) separately in Fukui et al. (2017).

5. CONCLUSIONS

In the present paper, we discussed the amount of the interstellar hydrogen gas and HI optical depth in the Perseus region by using the dust emission parameters obtained *Planck*, HI 21 cm line, and CO line data. The results are as follows:

1. The distributions of the data points on the τ_{353} – W_{HI} plot systematically vary by the change in T_{d} . This is consistent with the results in Fukui et al. (2014, 2015), which is that HI optical depth cannot be ignored for the low- T_{d} points. However, since the distance to the Perseus region is larger than that to the region analyzed in Fukui et al. (2014, 2015) and there exist the SFRs, the τ_{353} – W_{HI} plot is somewhat complicated as compared with the local clouds. As described in Section 3.4, the previous studies (Fukui et al. 2012, 2015) showed that the total hydrogen amount can be explained without assuming the presence of “CO-dark H_2 gas”. Therefore, we consider that the bad correlation between τ_{353} and W_{HI} for the low- T_{d} points is due to optically-thick HI gas.
2. In order to consider the dust evolution at high density regions, we calibrated the τ_{353} – N_{H} relationship by using the extinction at *J*-band. As with Roy et al. (2013), we confirmed that τ_{353} becomes larger as a function of the 1.3-th power of N_{H} ($\alpha = 1.3$). In addition, we reconsidered the reference values of τ_{353} and N_{H} in Equation (2) by referring to the results in Fukui et al. (2014). The calibrated τ_{353} – N_{H} relationship (Equation (3)) yields $\sim 20\%$ smaller N_{H} than that in the case of $\alpha = 1.0$. By using this relationship we can calculate N_{H} from τ_{353} more accurately, taking the dust evolution into account.
3. Compared with the present method, the conventional method which assumes that the HI gas is optically-thin, underestimates the amount of the hydrogen gas to be $\sim 62\%$ in the Perseus region. Optical depth of the HI gas (τ_{HI}) and spin temperature (T_{s}) can be calculated, and we obtain $\langle \tau_{\text{HI}} \rangle \sim 0.92$. These results support that there exists a large amount of optically-thick HI gas around the molecular clouds. The arguments by Fukui et al. (2014, 2015) still hold in the region where the density is relatively high and there exist the SFRs.
4. By using N_{H} calculated from τ_{353} and the CO intensity (W_{CO}), we estimated the spatial distribution of X_{CO} . We obtained $\langle X_{\text{CO}} \rangle \sim 1.0 \times 10^{20} \text{ cm}^{-2} \text{ K}^{-1} \text{ km}^{-1} \text{ s}$, which is consistent with the conventional value in the Galaxy, $X_{\text{CO}} \sim (1\text{--}2) \times 10^{20} \text{ cm}^{-2} \text{ K}^{-1} \text{ km}^{-1} \text{ s}$. The relative uncertainty in X_{CO} is smaller than conventional estimation and that in previous studies, typically 10–50%. Although the result in Lee et al. (2012, 2014) is underestimated to be $\sim 40\%$ compared to this result, this discrepancy in the X_{CO} maps can be quantitatively explained by the difference of the data used in order to calculate N_{H} , the effect of the optical depth of HI, and the difference of the integrated velocity ranges of HI 21 cm spectra.
5. We compared our τ_{HI} with that obtained in Stanimirović et al. (2014). When the optical depth is calculated based on the absorption measurements toward the background point sources, it can be underestimated to be $\sim 40\%$ on the average compared to that obtained based on the gas/dust emission data. It is revealed that the cold HI gas (CNM) has highly filamentary distribution by numerical simulation studies (e.g., Inoue & Inutsuka 2012). Therefore, the probability with which the optically-thick HI filaments lie on the infinitesimal

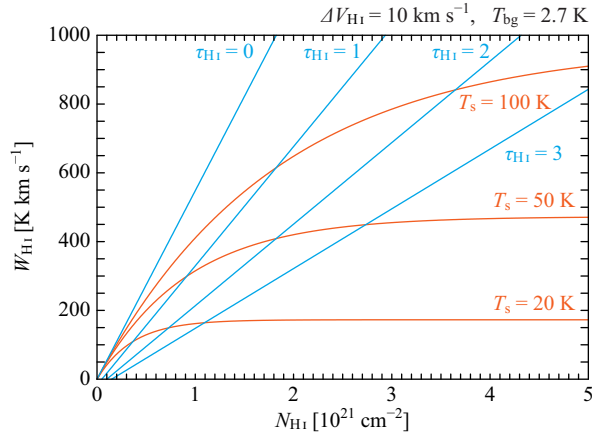


Figure 17. Theoretical curves of W_{HI} as functions of N_{HI} . The light-blue ones are for the case of fixing $\tau_{\text{HI}} = 0, 1, 2, 3$, and the orange ones $T_s = 20, 50, 100$ K. $\Delta V_{\text{HI}} = 10 \text{ km s}^{-1}$ and $T_{\text{bg}} = 2.7$ K are assumed.

apparent-size sources is small, $\sim 30\%$. The underestimation of τ_{HI} in absorption measurements is consistent with this picture.

This work was financially supported by Grants-in-Aid for Scientific Research (KAKENHI) of the Japan society for the Promotion of Science (JSPS) Grant Numbers 15H05694, 25287035.

This research has made use of NASA’s Astrophysics Data System. This publication utilizes data from Galactic ALFA HI (GALFA HI) survey data set obtained with the Arecibo L -band Feed Array (ALFA) on the Arecibo 305m telescope. Arecibo Observatory is part of the National Astronomy and Ionosphere Center, which is operated by Cornell University under Cooperative Agreement with the U.S. National Science Foundation. The GALFA HI surveys are funded by the NSF through grants to Columbia University, the University of Wisconsin, and the University of California. Based on observations obtained with *Planck* (<http://www.esa.int/Planck>), an ESA science mis-

sion with instruments and contributions directly funded by ESA Member States, NASA, and Canada. We acknowledge the use of the Legacy Archive for Microwave Background Data Analysis (LAMBDA), part of the High Energy Astrophysics Science Archive Center (HEASARC). HEASARC/LAMBDA is a service of the Astrophysics Science Division at the NASA Goddard Space Flight Center. This research has made use of the NASA/IPAC Infrared Science Archive, which is operated by the Jet Propulsion Laboratory, California Institute of Technology, under contract with the National Aeronautics and Space Administration. The CO line data was obtained with the CfA (Harvard-Smithsonian Center for Astrophysics) 1.2 m telescope (Dame et al. 2001). The $\text{H}\alpha$ emission data was assembled from the Wisconsin H-Alpha Mapper (WHAM), the Virginia Tech Spectral-Line Survey (VTSS), and the Southern H-Alpha Sky Survey Atlas (SHASSA) (Finkbeiner 2003). Some of the results in this paper have been derived using the HEALPix (Górski et al. 2005) package.

APPENDIX

A. DETERMINATION OF $\tau_{353,\text{ref}}$ AND $N_{\text{H},\text{ref}}$

$\tau_{353,\text{ref}}$ and $N_{\text{H},\text{ref}}$ are the normalization constants conveniently introduced in order to nondimensionalize the both sides of Equation (2). Although in Fukui et al. (2015) $\tau_{353,\text{ref}}$ and $N_{\text{H},\text{ref}}$ are determined as 4.77×10^{-6} and $1 \times 10^{21} \text{ cm}^{-2}$, respectively, we derive our $\tau_{353,\text{ref}}$ and $N_{\text{H},\text{ref}}$ for the Perseus region by using Equation (7). By giving α , τ_{HI} , and using $N_{\text{H},\text{ref}} = (1.15 \times 10^8) \times X_{\text{HI}} \times \tau_{353,\text{ref}}$ (Fukui et al. 2015) we make the free parameter in Equation (7) $\tau_{353,\text{ref}}$ alone, and determine it from the τ_{353} - W_{HI} plot. First, we describe the estimation of τ_{HI} for high- T_{d} points in the Perseus region.

Figure 17 shows theoretical relationships between N_{HI} and W_{HI} in the cases of fixing $\tau_{\text{HI}} = 0, 1, 2, 3$ or $T_s = 20, 50, 100$ K. We assumed that $\Delta V_{\text{HI}} = 10 \text{ km s}^{-1}$ and $T_{\text{bg}} = 2.7$ K. One can see that the variation width in W_{HI} becomes larger when τ_{HI} becomes higher even if T_s is a constant (orange curves).

Figure 18 is a τ_{353} - W_{HI} correlation plot (similar to Figure 6 in the present paper) for the MBM 53, 54, 55 and HLC G92–35 region (Fukui et al. 2014; Yamamoto et al. 2003). Although Figure 18 is almost the same as one in

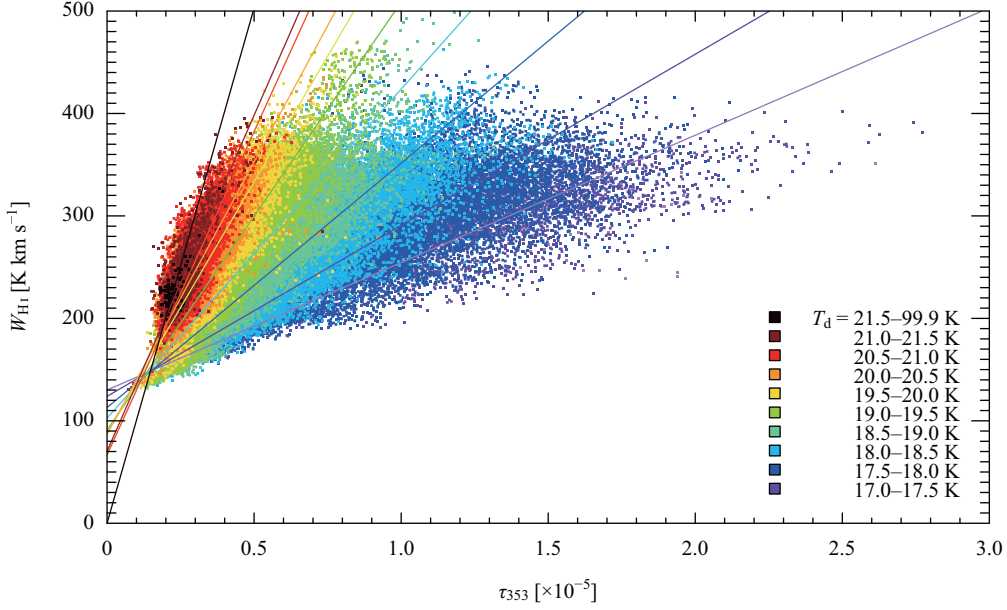


Figure 18. A τ_{353} - W_{HI} correlation plot in the MBM 53, 54, 55/HLCG 92–35 region (Fukui et al. 2014) colored by T_d . We used the *Planck* dust data R1.20 unlike Fukui et al. (2014). The results of RMA (reduced major axis) regressions for each T_d range are also plotted. We assumed that H I gas is optically-thin for the data points of $T_d \geq 21.5$ K (Fukui et al. 2014), therefore we make the regression line for $T_d \geq 21.5$ K pass through the origin.

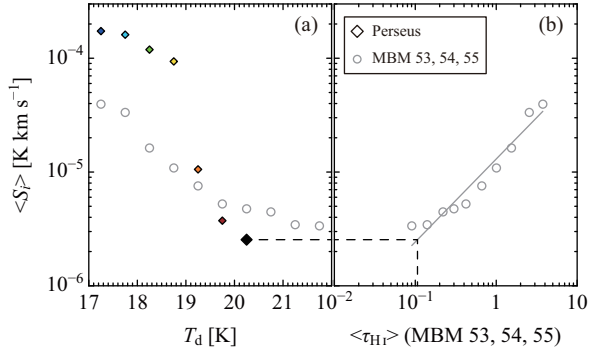


Figure 19. (a) Dispersions of the data points for each T_d range. The open circles indicate the results for the MBM 53, 54, 55 region and we use this as a template. The diamonds indicate the result for the Perseus region. The colors of the diamonds are the same as Figure 20. (b) The relationship between $\langle \tau_{\text{HI}} \rangle$ (average of τ_{HI} derived by the same method as Fukui et al. 2014) and the variance for each T_d range (MBM 53, 54, 55 template). The solid line indicates the result of a linear fit. The horizontal dashed line denotes $\langle S_i \rangle$ for the range of $T_d > 20.0$ K, and the vertical dashed line the corresponding $\langle \tau_{\text{HI}} \rangle$ ($= 0.11$).

Fukui et al. (2014), the *Planck* dust data R1.20 are used and we apply an additional mask which excludes the data points where intermediate-velocity clouds (Pegasus-Pisces Arch, Albert & Danly 2004) are detected in Figure 18. If we regard τ_{353} as a tracer of N_{H} and if there is a positive correlation relationship between T_d and T_s , Figure 17 and 18 can roughly be considered as the same thing. Since it is thought that τ_{HI} is larger if T_d is lower, the variation width in W_{HI} for the low- T_d points is relatively large in Figure 18, and vice versa. Accordingly, we performed linear fittings for each T_d range and examined variances from each regression line. We used the reduced major axis (RMA) regression method (e.g., Isobe et al. 1990), which minimizes the sum of the areas of the right-angled triangles delimited by each data point and the regression line, $\sum S_i$, and we defined the variance as the mean of the areas of the triangles, $\langle S_i \rangle$.

The results are shown in Table 3 and in Figure 19. In the MBM 53, 54, 55 region, an anti-correlation relationship between T_d and $\langle S_i \rangle$ can obviously be seen (the columns 1 and 2 of Table 3, and Figure 19(a)). The column 3 of Table 3 shows the mean τ_{HI} values for each T_d range derived by using the method described in Fukui et al. (2014), and we can see a positive correlation relationship against $\langle S_i \rangle$ (see also Figure 19(b)). Therefore, $\langle \tau_{\text{HI}} \rangle$ for $T_d \geq 20.0$ K for

Table 3. Relationship between T_d , $\langle S_i \rangle$, and $\langle \tau_{\text{HI}} \rangle$

	MBM 53, 54, 55		Perseus
T_d	$\langle S_i \rangle$	$\langle \tau_{\text{HI}} \rangle$	$\langle S_i \rangle$
[K]	[10^{-5} K km s $^{-1}$]		[10^{-5} K km s $^{-1}$]
(a)	(b)	(c)	(d)
$21.5 \leq$	0.34	0.09	...
21.0–21.5	0.34	0.14	...
20.5–21.0	0.45	0.22	...
20.0–20.5	0.48	0.30	0.25
19.5–20.0	0.52	0.42	0.37
19.0–19.5	0.76	0.66	1.1
18.5–19.0	1.09	1.01	9.4
18.0–18.5	1.63	1.54	11.9
17.5–18.0	3.34	2.56	16.1
< 17.5	3.95	3.76	17.3

NOTE—The dispersions of the data points from the regression lines shown in Figure 18. (a) The T_d range. (b) and (c) The dispersions of the data points defined in the text, and the mean value of τ_{HI} estimated in Fukui et al. (2014). We use the relationship between these two as a template. (d) The dispersions of the data points in the Perseus region.

the Perseus region can be estimated by using the $\langle \tau_{\text{HI}} \rangle$ – $\langle S_i \rangle$ relationship for the MBM 53, 54, 55 region as a template. The solid line in Figure 19(b) indicates the result of a linear fitting for the $\langle \tau_{\text{HI}} \rangle$ – $\langle S_i \rangle$ relationship. By referring this line we get $\langle \tau_{\text{HI}} \rangle$ for $T_d \geq 20.0$ K for the Perseus region as $\langle \tau_{\text{HI}} \rangle = 0.11$ from $\langle S_i \rangle = 0.5 \times 10^{-5}$ K km s $^{-1}$ (the dashed lines).

By applying this $\langle \tau_{\text{HI}} \rangle$ into Equation (7) and with this function fitting the data points of $T_d \geq 20.0$ K, $\tau_{353,\text{ref}}$ for the Perseus region can be calculated. Note that $\alpha = 1.3$ was applied and we used the relationship of $N_{\text{H,ref}} = (1.15 \times 10^8) \times X_{\text{HI}} \times \tau_{353,\text{ref}}$ (Fukui et al. 2015). The result of the fitting is plotted in Figure 20, and we get $\tau_{353,\text{ref}} = 1.2 \times 10^{-6}$ and $N_{\text{H,ref}} = 2.5 \times 10^{20}$ cm $^{-2}$. The left-hand and right-hand dotted curves show the cases which $\tau_{353,\text{ref}} = 4.77 \times 10^{-6}$ (Fukui et al. 2015), and $\tau_{353,\text{ref}} = 8.7 \times 10^{-7}$ (corresponds to $W_{\text{HI}} = 100$ K km s $^{-1}$ in Fukui et al. 2015), respectively. Both of them cannot trace the distribution of the data points of $T_d \geq 20.0$ K.

From the above results, we adopted $\alpha = 1.3$, $\tau_{353,\text{ref}} = 1.2 \times 10^{-6}$, and $N_{\text{H,ref}} = 2.5 \times 10^{20}$ cm $^{-2}$ for the Perseus region.

REFERENCES

- Albert, C. E., & Danly, L. 2004, in *Astrophysics and Space Science Library*, Vol. 312, High Velocity Clouds, ed.
- H. van Woerden, B. P. Wakker, U. J. Schwarz, & K. S. de Boer, 73
- Bally, J., Walawender, J., Johnstone, D., Kirk, H., & Goodman, A. 2008, *The Perseus Cloud*, ed. B. Reipurth, 308
- Bolatto, A. D., Wolfire, M., & Leroy, A. K. 2013, *ARA&A*, 51, 207
- Cotten, D. L., & Magnani, L. 2013, *MNRAS*, 436, 1152

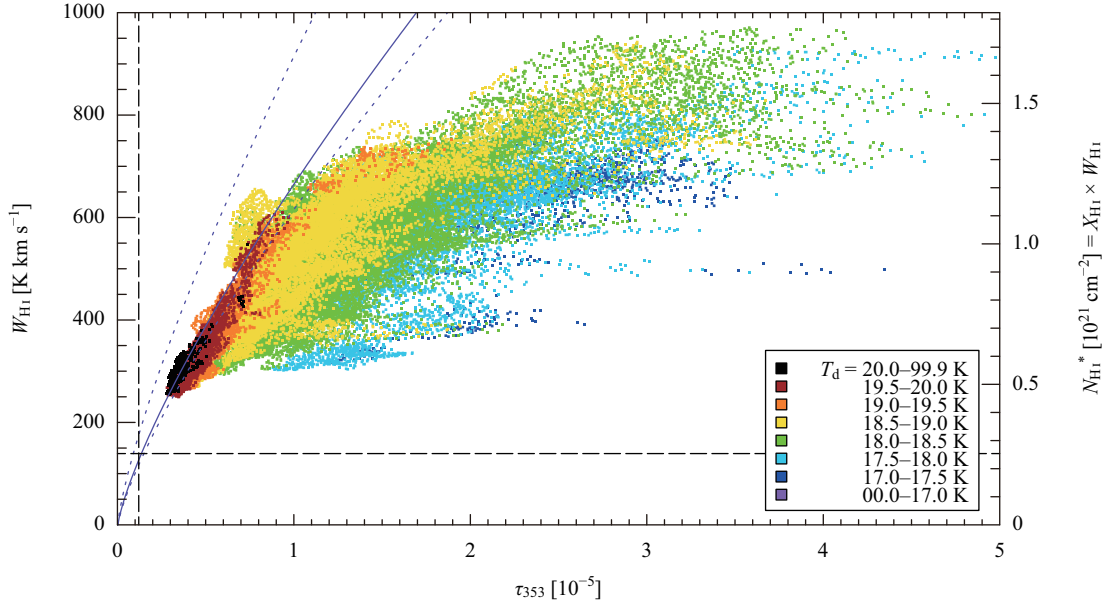


Figure 20. The τ_{353} - W_{HI} plot in the Perseus region. The right hand y -axis indicates the column number density of H I in the optically-thin limit (N_{HI}). Fitting the data points which $T_{\text{d}} > 20.0$ K with the theoretical function fixing $\alpha = 1.3$, and $\tau_{\text{HI}} = 0.11$, we get $\tau_{353,\text{ref}} = 1.2 \times 10^{-6}$. Note that we use the relationship described in Fukui et al. (2015), $N_{\text{H,ref}} = (1.15 \times 10^8) \times X_{\text{HI}} \times \tau_{353,\text{ref}}$. The left dotted curves indicates the case which $\tau_{353,\text{ref}} = 4.77 \times 10^{-6}$, and the right one the case which $\tau_{353,\text{ref}} = 8.7 \times 10^{-7}$. The dashed lines correspond to $\tau_{353,\text{ref}} = 1.2 \times 10^{-6}$ and $N_{\text{H,ref}} = 2.5 \times 10^{20} \text{ cm}^{-2}$.

Dame, T. M., Hartmann, D., & Thaddeus, P. 2001, *ApJ*, 547, 792
 Dickey, J. M., & Lockman, F. J. 1990, *ARA&A*, 28, 215
 Draine, B. T. 2011, *Physics of the Interstellar and Intergalactic Medium*
 Finkbeiner, D. P. 2003, *ApJS*, 146, 407
 Forbrich, J., Lada, C. J., Lombardi, M., Román-Zúñiga, C., & Alves, J. 2015, *A&A*, 580, A114
 Fukui, Y., Hayakawa, T., Inoue, T., et al. 2017, *ArXiv e-prints*, arXiv:1701.07129
 Fukui, Y., Torii, K., Onishi, T., et al. 2015, *ApJ*, 798, 6
 Fukui, Y., Sano, H., Sato, J., et al. 2012, *ApJ*, 746, 82
 Fukui, Y., Okamoto, R., Kaji, R., et al. 2014, *ApJ*, 796, 59
 Gillmon, K., Shull, J. M., Tumlinson, J., & Danforth, C. 2006, *ApJ*, 636, 891
 Górski, K. M., Hivon, E., Banday, A. J., et al. 2005, *ApJ*, 622, 759
 Heiles, C., & Troland, T. H. 2003, *ApJS*, 145, 329
 Inoue, T., & Inutsuka, S.-i. 2012, *ApJ*, 759, 35
 Isobe, T., Feigelson, E. D., Akritas, M. G., & Babu, G. J. 1990, *ApJ*, 364, 104
 Jones, A. P., Fanciullo, L., Köhler, M., et al. 2013, *A&A*, 558, A62
 Juvela, M., & Montillaud, J. 2016, *A&A*, 585, A38

Landsman, W. B. 1993, in *Astronomical Society of the Pacific Conference Series*, Vol. 52, *Astronomical Data Analysis Software and Systems II*, ed. R. J. Hanisch, R. J. V. Brissenden, & J. Barnes, 246
 Langer, W. D., Velusamy, T., Pineda, J. L., Willacy, K., & Goldsmith, P. F. 2014, *A&A*, 561, A122
 Lee, M.-Y., Stanimirović, S., Wolfire, M. G., et al. 2014, *ApJ*, 784, 80
 Lee, M.-Y., Stanimirović, S., Douglas, K. A., et al. 2012, *ApJ*, 748, 75
 Lombardi, M., & Alves, J. 2001, *A&A*, 377, 1023
 Magnani, L., Onello, J. S., Adams, N. G., Hartmann, D., & Thaddeus, P. 1998, *ApJ*, 504, 290
 McClure-Griffiths, N. M., Dickey, J. M., Gaensler, B. M., Green, A. J., & Haverkorn, M. 2006, *ApJ*, 652, 1339
 Miville-Deschênes, M.-A., & Lagache, G. 2005, *ApJS*, 157, 302
 Peek, J. E. G., Heiles, C., Douglas, K. A., et al. 2011, *ApJS*, 194, 20
Planck Collaboration, Ade, P. A. R., Aghanim, N., et al. 2011a, *A&A*, 536, A1
 —. 2011b, *A&A*, 536, A19
Planck Collaboration, Abergel, A., Ade, P. A. R., et al. 2011c, *A&A*, 536, A24
 —. 2014, *A&A*, 571, A11
 Rachford, B. L., Snow, T. P., Tumlinson, J., et al. 2002, *ApJ*, 577, 221

- Reich, P., & Reich, W. 1986, *A&AS*, 63, 205
- Reich, W. 1982, *A&AS*, 48, 219
- Ridge, N. A., Schnee, S. L., Goodman, A. A., & Foster, J. B. 2006, *ApJ*, 643, 932
- Roy, A., Martin, P. G., Polychroni, D., et al. 2013, *ApJ*, 763, 55
- Schultheis, M., Chen, B. Q., Jiang, B. W., et al. 2014, *A&A*, 566, A120
- Sofue, Y. 2013, *PASJ*, 65, 118
- Stanimirović, S., Murray, C. E., Lee, M.-Y., Heiles, C., & Miller, J. 2014, *ApJ*, 793, 132
- Tóth, L. V., Marton, G., Zahorecz, S., et al. 2014, *PASJ*, 66, 17
- Wenger, M., Ochsenbein, F., Egret, D., et al. 2000, *A&AS*, 143, 9
- Wolfire, M. G., Hollenbach, D., & McKee, C. F. 2010, *ApJ*, 716, 1191
- Yamamoto, H., Onishi, T., Mizuno, A., & Fukui, Y. 2003, *ApJ*, 592, 217
- Ysard, N., Köhler, M., Jones, A., et al. 2015, *A&A*, 577, A110